MICROSTRUCTURE CHARACTERIZATION OF PULSED LASER DEPOSITED METAL OXIDE NANOPARTICLES

Thesis author	_____
	Samuli Komulainen
Thesis supervisor	_____
	Jyrki Lappalainen
Second examiner	_____
	Jarkko Puustinen
Technical advisor	_____
	Joni Huotari
Accepted	____/____2016
Grade	_____

ABSTRACT

In this thesis, the effects of pulsed laser deposition processing parameters on microstructure of tungsten trioxide thin films was studied. Samples were deposited at room temperature under three different background oxygen pressure levels using three different laser beam fluence. Some samples were post-annealed at temperatures between 400 and 600 °C, and the rest were left as deposited. Micro- and crystal structure of the samples were examined with X-ray diffraction, Raman spectroscope, atomic force microscope, and field emission scanning electron microscope. Results showed that the films were porous, constructed of nanoparticles and had a rough surface. In crystal structure studies, amorphous phase as well as crystalline monoclinic γ- ja ε-phases were found.

   Value of background pressure and laser beam fluence were found to have significant effect on crystal structure, morphology, porosity, and thickness of the films. Effect of post-annealing temperature was non-linear and dependent on the as-deposited structure of the films. Before the post-annealing, the films were mostly amorphous and during the heating some of them remained amorphous, some crystallized into γ-phase, and some formed different mixtures of γ- and ε-phases. Grain sizes of the samples were studied with different methods, which gave somewhat different results, but it could be concluded that fluence of the laser was largely insignificant, and pressure and post-annealing temperature had more dominant effects.

Key words: pulsed laser deposition, tungsten trioxide, crystal structure, surface morphology, nanoparticles

TIIVISTELMÄ

Tässä työssä tutkittiin pulssilaserkasvatuksen parametrien vaikutusta volframitrioksidistaohutkalvojen mikrorakenteeseen. Näytteet kasvatettiin huonelämpötilassa kolmessa eri happipaineessa ja kolmella eri laserin intensiteetillä. Osa näytteistä jälkihehkutettiin 400-600 °C asteen lämpötilassa. Näytteiden mikro- ja kiderakennetta tutkittiin röntgendiffraktiolla, Raman spektroskopialla sekä atomivoima- ja elektronimikroskopian menetelmillä. Tuloksista kävi ilmi kalvojen huokoinen, nanopartikkeleista koostuva rakenne, pinnan karheus sekä eri faasien määräsuhteet. Amorfisen faasin lisäksi näytteistä löytyi kiteiset monokliiniset γ- ja ε-faasit.

Taustapaineen ja laserin intensiteetin muutosten havaittiin vaikuttavan voimakkaasti kalvojen huokoisuuteen, pinnan rakenteeseen ja kalvon paksuuteen. Paineen ja intensiteetin vaikutukset olivat vastakkaisia, mutta aina samanlaisia. Jälkihehkutuksen vaikutus oli epälineaarinen sekä riippuvainen hehkutuslämpötilasta, mutta myös hehkuttamattomasta kalvon rakenteesta. Ennen jälkihehkutusta kalvot olivat pääsääntöisesti amorfista faasia, mutta hehkutettaessa osa jäi pääosin amorfiseksi ja loput kiteytyivät melko puhtaaksi monokliiniseksi γ-faasiksi tai erilaiseksi yhdistelmäksi ε- ja γ-faaseja. Jälkihehkutettujen kalvojen raekokoja laskettiin röntgendiffraktion mittaustuloksista eri menetelmillä, joilla saatiin hieman eriäviä tuloksia, mutta kaikista kävi ilmi, että laserin intensiteetillä ei ollut merkittävää vaikutusta keskimääräiseen raekokoon toisin kuin lämpötilalla ja taustapaineella.

Avainsanat: pulssilaserkasvatus, volframitrioksidi, kiderakenne, pinnan morfologia, nanopartikkelit

TABLE OF CONTENTS

FOREWORDS

This thesis was done in facilities of Microelectronics and Materials Physics Laboratories during the late 2014 and early 2015 as a part of SENSIndoor project.

I would like to thank the supervisor of this work, Prof. Jyrki Lappalainen for giving me this opportunity and for his help and expertise on theoretical and practical problems I had. I would also like to thank DI Joni Huotari and Dr. Jarkko Puustinen for helping and tutoring me especially through the beginning, as well as Tomi Haapalainen for lending me his measurement data on gas sensing parts. A thank goes to whole personnel of our laboratory for refreshing and humorous atmosphere, which was a welcomed alternation for the quiet writing process.

Last, but not least, I would like to thank my family and friends for believing in me all these years and for the encouragement.

Oulu 5.5.2016

Samuli Komulainen

LIST OF ABBREVIATION AND SYMBOLS

a, b, c	lattice parameters
d	distance between diffraction planes
E	amplitude of an electromagnetic wave
h	Planck's constant
k	Boltzmann's constant
l	order of reflection
n	refractive index
R_q	rms roughness parameter
T	temperature
$t(\beta)$	film thickness scattered in angle β
t_{max}	maximum film thickness
U_i	first ionization potential of gas atoms
v	frequency
Z	elemental charge of ion
α_{IB}	absorption coefficient
δ	skin depth
ε_0	permittivity of free space
θ	angle between diffracted beam and diffraction plane
λ	wavelength
μ_0	permeability of free space
ρ_i	density of singly charged ions in cm^3
ρ_n	density of neutrals in cm^3
σ	electrical conductivity
Φ	power density
ω	angular frequency
2D-FFT	2-dimensional fast Fourier transformation
AFM	atomic force microscopy
CO	carbon monoxide
FESEM	field emission scanning electron microscopy
GID	grazing incidence diffraction
H_2S	hydrogen-sulfide
NH_3	ammonia
NO_x	nitrogen-oxides
O	oxygen
PLD	pulsed laser deposition
PSD	power spectral density
RT	room temperature
SiO_2	silicon dioxide
W_xO_y	tungsten oxides

WO$_3$	tungsten trioxide
XRD	X-ray diffraction

1.   INTRODUCTION

The history of gas sensor industry is relatively young. The first resistive gas sensor was introduced in 1962. It was based on oxide semiconductor, which resistance changed in presence of gas, a phenomenon that was discovered almost a decade earlier. Real era of the industry started in 1970's when semiconductor based combustion gas sensors, solid electrolyte oxygen sensors, and humidity sensors were commercialized for non-professional use. Although the gas sensor industry is still relatively small compared to other sensors, it is growing quickly as the area of use is expanding rapidly. During this millennium, the industry has spread to environmental protection, medical institutes, and procession of groceries to name a few. The demand of cheap and reliable sensors for measuring the quality of indoor air drives research of both materials and manufacturing techniques [1].

Low price, extremely high sensitivity, small size, low power consumption, and wide variety of materials with different physical, chemical, and optical characteristics make semiconducting metal oxides interesting and potential development and research topic, even though there still are challenges in selectivity and stability. The properties of gas sensing abilities are highly dependent on the structure of the material. The gas sensitivity, and even selectivity, of a semiconductor can be greatly enhanced by controlling the morphology and microstructure, such as average grain size [2, 3]. This drives the development of better manufacturing techniques and research for better understanding of the existing properties.

One of the potential manufacturing methods is pulsed laser deposition (PLD), which started in 1960's when first high-powered ruby laser became available. The first high-powered ruby laser triggered the development of PLD. After a few years of theoretical and experimental studies, first thin film deposition using intense laser radiation was demonstrated. After a fast beginning, the next two decades were much slower. The first major breakthrough came in the mid-1970's when electronic Q-switch technique enabled delivery of short pulses with high peak power density. The second breakthrough, which really made PLD interesting, came in 1987 by the growth of high temperature superconducting films [4]. During the late 1980's and early 1990's it was discovered that, in presence of ambient gas, the PLD produces porous structure consisting of nanosized particles that were later found to be useful in gas detecting [5].

The purpose of this thesis is to study the effects of PLD parameters on microstructure of tungsten trioxide (WO_3) thin films deposited on silicon substrate. Principles and theory of PLD are explained in Chapter 2, properties of tungsten trioxide in Chapter 3, and measurement techniques in Chapter 4. Used equipment and methods are explained in Chapter 5. The measurement data is presented and discussed in Chapter 6 and final conclusions of the work are drawn in Chapter 7.

2.   PULSED LASER DEPOSITION

2.1. Setup

The PLD setup consists of laser and necessary optics, reaction chamber, vacuum pump, substrate, and target as illustrated in Fig. 1 [6]. Target and substrate are placed perpendicular to each other and the chamber is evacuated by the pump into vacuum. Afterwards, the chamber can be filled with either inert or reactive background gas. Laser beam is focused on surface of the target and the short pulses will evaporate and ionize material from target. Formed plasma plume expands and reaches the substrate with enough kinetic energy for strong adhesion of the growing film [7].
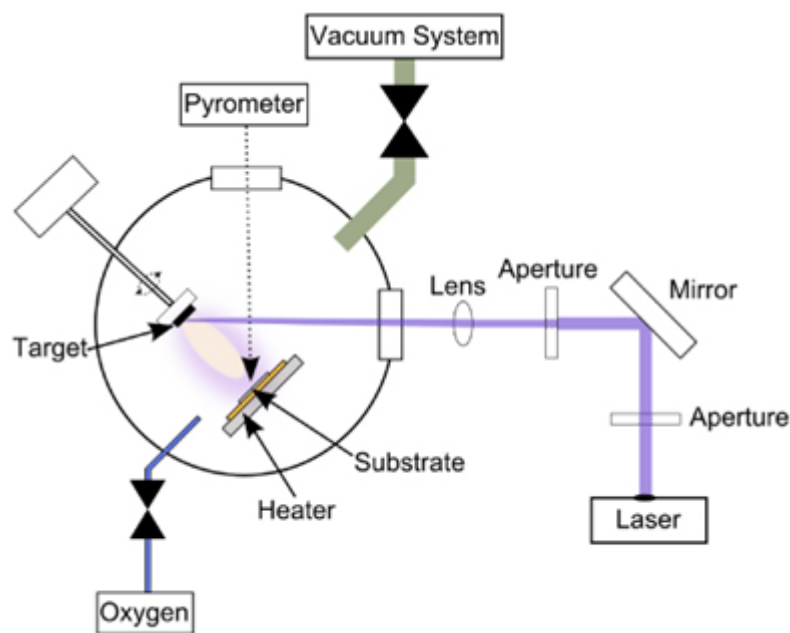
Figure 1. PLD setup scheme. Modified from Schilling.

2.2. Laser-Target Interactions

The electromagnetic energy of the laser radiation is converted into electronic excitation immediately when the laser beam is absorbed into the target. Electric field amplitude E of an electromagnetic wave is:

$$E = \sqrt{2\Phi/cn\varepsilon_0} \tag{1}$$

where Φ is the power density, ε_0 is the permittivity of free space, c is the velocity of light, and n is the refractive index.

   If the strength of the electric field is greater than threshold value of the material, dielectric breakdown will occur through electron excitation above work function level, leading to pure ablation process. However, in most cases thermal diffusion controls

the material removal as it only takes ~10 ps for electrons to start transferring their kinetic energy into the lattice of the bulk material. The exact time needed depends on physical properties of used material.

With sufficient fluence, ablation and vaporization of material within the absorption depth will begin about 100 ps after the first photons have reached target material. From here on, the forming plasma absorbs most of the remaining laser pulse energy becoming more ionized, whereas the bulk material is largely screened by the plasma. This process is called laser supported absorption and it can produce plasma species with kinetic energies up to 100 eV, but it has low ablation yield, especially for materials with high optical absorption coefficient [8].

2.3. Laser-Plasma Interactions

The nascent plasma absorbs laser radiation in form of inverse Bremsstrahlung. The absorptivity α_{IB} follows equation:

$$\alpha_{IB} = 3{,}7 \times 10^8 \frac{Z^3 \rho_i^2}{v^3 \sqrt{T}} \left(1 - e^{-\frac{hv}{kT}}\right) \tag{2}$$

where $Z = 1$ is elementary charge of the ion, ρ_i is density of singly charged ions in cm^3, T is gas temperature in Kelvins, v is frequency of radiation, h is Planck's constant, and k is Boltzmann's constant.

For a gas in local thermal equilibrium, the density of singly charged ions per cubic centimeter can be calculated using Saha equation:

$$n_i = \sqrt{2{,}4 \times 10^{15} T^{3/2} \rho_n e^{-U_i/kT}} \tag{3}$$

where ρ_n is density of neutrals in cm^3 and U_i is the first ionization potential of the gas atoms in electron volts.

As the plasma cloud absorbs radiation it becomes hotter and more ionized, which increases the absorptivity, but the ionization degree drops due to recombination as the plasma expands. Thus the travelling plasma is mostly transparent and most of the absorption occurs near the target, where the density of free electrons is higher.

Experiments have shown that the ionization degree of plasma is between 0.1 and 1 immediately after the laser pulse has extinguished. Using equation (3), a temperature in order of 10 000 K is needed to achieve such degree of ionization. In addition, non-thermal desorption and ionization processes can create locally high concentrations of electrons. These local non-uniformities with higher free electron density can be caused by laser focus "hot spots", multiphoton ionization or statistical variations, which can generate a runaway breakdown of the entire plasma cloud in few femtoseconds [7, 8].

2.4. Plasma Expansion

The nascent plasma forms a thin high density Knudsen layer, where thermal equilibrium is preserved via collisions of particles. The velocity of particles follow drifted Maxwellian distribution. Collisions alter the velocity components and up to 20 % of the particles can end up travelling back to the target and re-condensate [8, 9].

Part of the plasma's internal energy is thermally coupled to the surface of the target causing melting and vaporization. For metals, even one third of the total photonic energy can be wasted in heating the bulk material. Because of melting and re-condensation cycles, the target's surface morphology changes under the laser bombardment making it necessary to stress a never before used target prior to the first actual deposition.

As the plasma plume starts to expand into vacuum the angular distribution follows cosine-power law:

$$t(\beta) = t_{max}cos^{p+3}(\beta) \tag{4}$$

where t is film thickness, β is angle measured from the target surface normal measured at the center of the laser spot, p is integer, and t_{max} is maximum film thickness. For multicomponent target, different elements may have different angular dependencies [4].

The expanding process is adiabatic after the laser beam has extinguished and new particles are no longer emitted from the target. The temperature of the plasma decreases as the volume of the plume increases and the thermal energy is converted into kinetic energy of the particles. The cooling of the plasma is very rapid during the first 100 ns, but starts to slow down afterwards due to energy being retrieved in recombination of ions and electrons. The plasma typically cools to a temperature of 3000 - 5000 K and the kinetic energies can range from 1 - 500 eV, but are usually in range of 5 - 50 eV. The kinetic energies depend heavily on the fluence of the laser, which also effects on the exponent p of the cosine-power function [10].

The expansion of the plasma is greatly affected by background gas that is often used in PLD chamber. Particles ejected from the target collide with ambient gas which shapes, and even splits, the plasma plume and reduces the energy of the particles. The Figs. 2-4 illustrate the difference in shape and expansion of the plume under different background pressure [6]. Background gas can also be used as a reactant. Usually oxygen is used for this purpose. In vacuum, the plume expands freely and finally reaches some constant velocity, but in presence of background gas, the velocity starts to diminish after the initial acceleration. [7, 10].
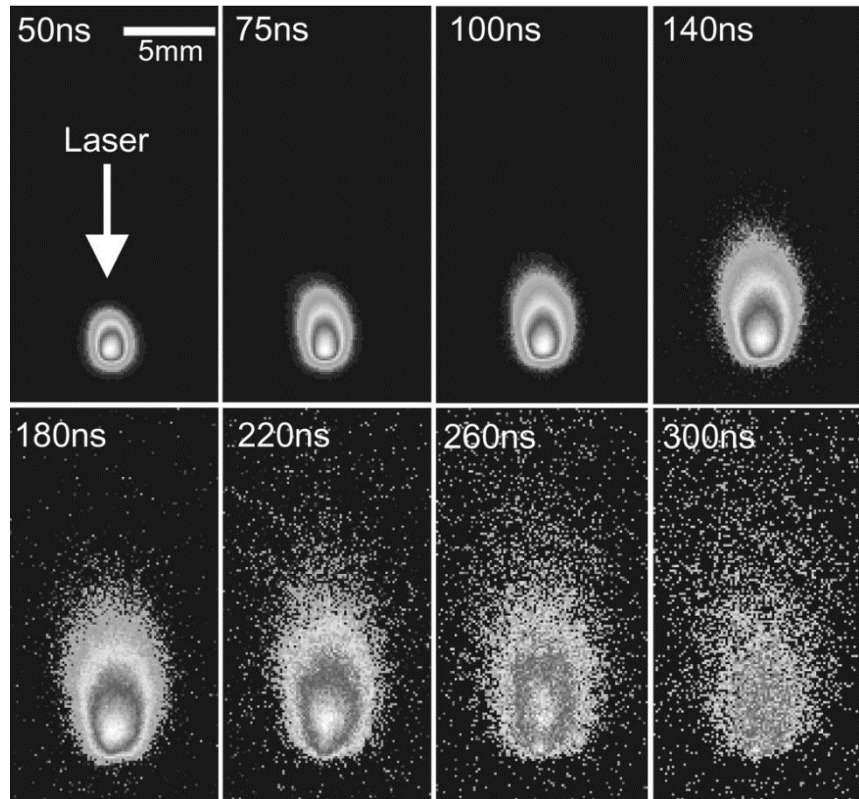
Figure 2. Expansion of laser-produced aluminum plasma plume in base pressure of 10^{-6} Torr.
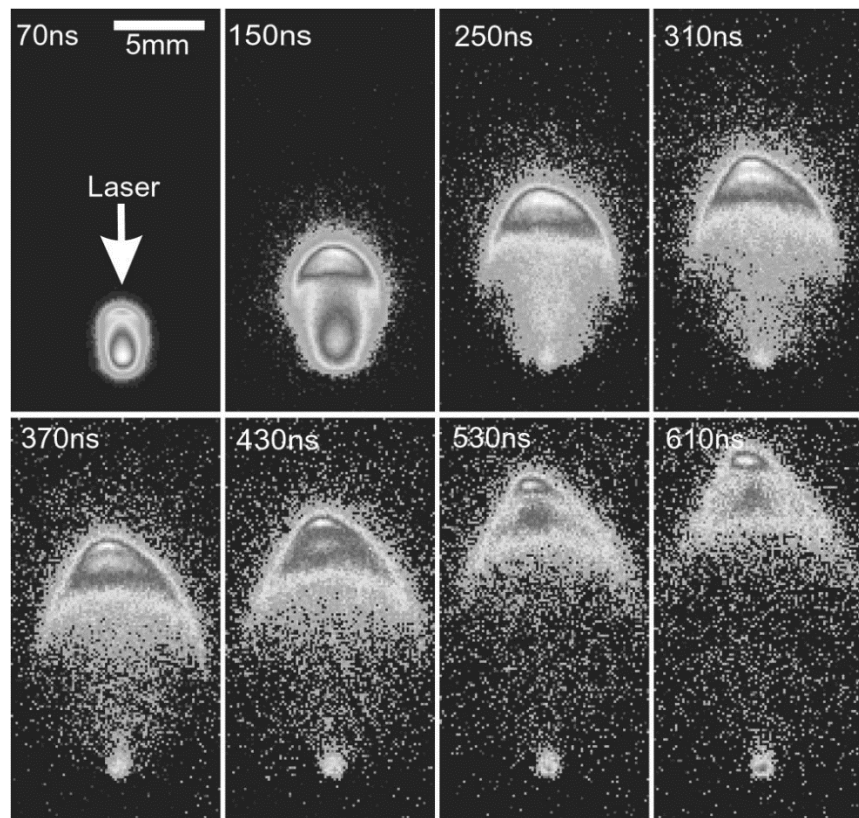

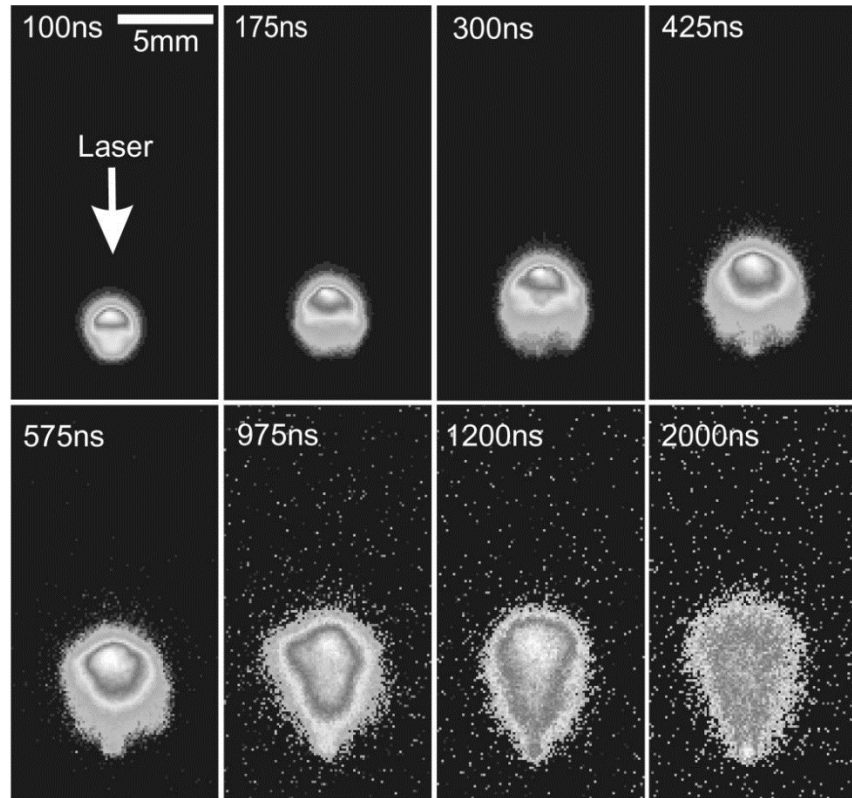Figure 3. Expansion of laser-produced aluminum plasma plume under background air pressure of 150 mTorr.

Figure 4. Expansion of laser-produced aluminum plasma plume under background air pressure of 10 Torr.

2.5. Particle and Droplet Generation

With high enough ambient gas pressure, expansion of plasma plume through the gas creates a shock front. Through multiple collisions with background gas, the particles in plasma dissipate kinetic energy. When the particles slow down sufficiently, they start to nucleate and form nanoparticles in the shock front. The shock fronts are short-lived and thus the size of the nanoparticles remain small. In presence of even higher pressure, the nanoparticles slow down enough to form stable agglomerates that survive the collision when they hit the substrate. This kind of agglomerates may vary in size from nanometers to microns [8, 11, 12].

Droplet generation impairs the morphology of deposited structure. Droplet generation is caused by three phenomena: subsurface explosion, recoil ejection, and exfoliation. Subsurface explosion takes place in materials, where the time needed to evaporate surface layer is longer than time needed to convert laser energy into heat and transfer it to the bulk. The surface layer is defined by having a thickness of the order of skin depth δ:

$$\delta = \sqrt{2/\mu_0 \sigma \omega} \tag{5}$$

where μ_0 is permittivity of free space, σ is electrical conductivity, and ω is angular frequency of the incoming light.

Subsurface explosion produces micron-sized droplets, but is usually negligible in dielectric materials as electrical and thermal conductivities are small. On the contrary, subsurface explosion may be dominant in metals with high thermal conductivity and low melting temperature, and can only be avoided by using very short pulses or low laser fluence, which reduces the ablation yield.

Recoil ejection, also known as a piston effect, occurs when expanding plasma plume presses transient melt onto the solid bulk. The bulk material in contact with initial plasma can endure recoil forces of up to 10 kN during laser pulse. The recoil ejected droplets are similar in size with the ones caused by subsurface boiling and it is difficult to identify them.

Exfoliation is a hydrodynamic effect caused by repeated melt-freeze cycles of the target that increase the surface roughness. This results generation of macroscopic outgrowths that become thermally decoupled and necked off before finally breaking away as particulates. Exfoliation can easily be prevented by moving the target in a way that consecutive laser pulses hit different spots of the target [8].

2.6. Film Growth

Particles ablated from the target hit the substrate and attach to it as illustrated in Fig. 5 [7]. Surface diffusion and desorption of particles may occur, but mostly a strong adhesion is formed by the kinetic energy of the particles. The film growth mode can be Volmer-Weber type nucleation and formation of islands, Frank-van der Merwe type monolayer growth or Stranski-Krastanov type monolayer growth followed by formation of islands. Growth process depends on processing parameters and materials used [4].
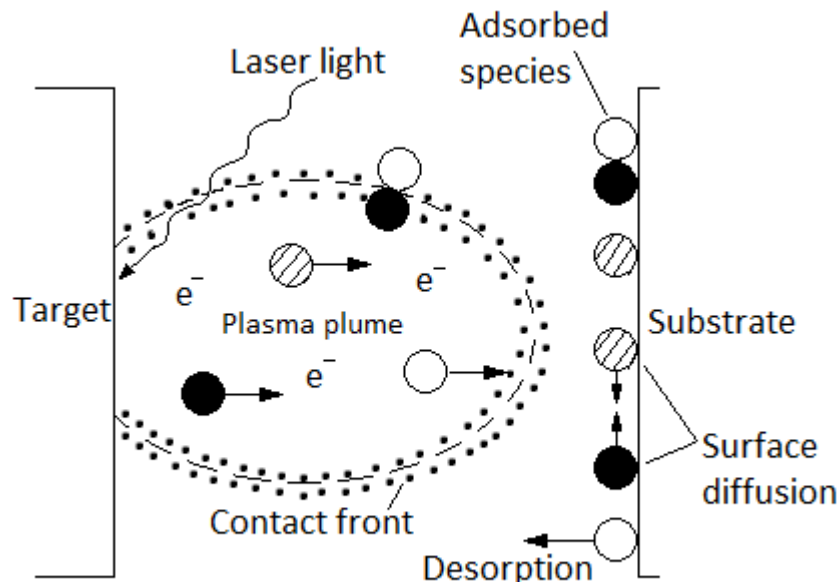

Figure 5. Schematic description of laser ejected particles hitting the surface of the substrate. Modified from Bäuerle.

In presence of ambient gas, the process is different as energy of particles is reduced by collisions with background gas and they can form stable nanoparticles and even agglomerates which can survive the impact with substrate. This results to lower adhesion and porous structure that resembles nanopowder rather than thin film with high density [7, 11].

2.7. Post-annealing

The films can be heated after deposition. Post-annealing is used to crystallize the deposited amorphous material, but it can also cause phase transitions, as well as alter the structure and morphology through Ostwald ripening and thermal diffusion. The average grain size is increased as a function of annealing temperature and duration. Post-annealing can also create oxygen vacancies that may improve the gas sensing response of the material [13, 14, 15].

3. TUNGSTEN TRIOXIDE

Tungsten trioxide (WO_3) is widely studied material in gas sensing. It has a downside of being unstable, but it has excellent sensitivity to various gases such as nitrogen oxides NO_x, H_2S, and NH_3 gases [16]. WO_3 is also used in other areas such as electrochromics [17].

3.1. Structure

Tungsten trioxide is based on the [WO_6] octahedron units with average W—O bond length of about 1.9 Å. WO_3 units are connected by corner sharing. Because the units can be connected along different directions, WO_3 has one type of amorphous phase and 5 different crystalline phases. In amorphous phase, the [WO_6] units do not have a regular pattern. The stable crystalline phases include monoclinic, triclinic, orthorhombic, and tetragonal ones as can be seen from Table 1. Structure of the most common WO_3 phases is illustrated in Fig. 6 [18]. Although the bulk ε-phase is stable only below -40 °C, it is possible to produce WO_3 that has stable ε-phase co-existing with γ-phase at room temperature [18, 19, 20, 21].

Table 1. Properties of WO_3 phases.

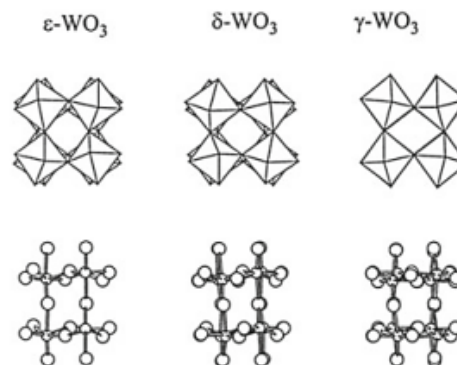| Structure	Symbol	Existing temperature (°C)	Space group	Lattice parameters
Monoclinic	ε	< -40	Pc	a = 5.278 Å, b = 5.156 Å, c = 7.664 Å, $β$ = 91.762°
Triclinic	δ	-40 - 17	$P\bar{1}$	a = 7.310 Å, b = 7.524 Å, c = 7.685 Å, $α$ = 88.850°, $β$ = 90.913°, $γ$ = 90.935°
Monoclinic	γ	17 - 320	$P2_1/n$	a = 7.301 Å, b = 7.538 Å, c = 7.689 Å, $β$ = 90.893°
Orthorhombic	β	320 - 720	Pmnb	a = 7.341 Å, b = 7.570 Å, c = 7.754 Å
Tetragonal	α	720 - 900	P4/nmm	a = 5.250 Å, c = 3.915 Å

Figure 6. Structure of some of the WO_3 phases.

3.2. Gas Sensing Properties

In gas sensing experiments, WO_3 has been found to be sensitive to nitrogen oxides. In the case of strong ε-phase in addition to γ-phase in WO_3, the composition was found to have lower sensitivity for NO_x, almost no sensitivity for CO, but a high response and thus selectivity for acetone. It has been suggested that the asymmetric structure of ε-phase has an important role in the selective detection of acetone. ε-phase is the only ferroelectric phase of WO_3, which alone makes it interesting [19, 22].

4. MEASUREMENT THEORY

4.1. Atomic Force Microscopy

Atomic force microscopy (AFM) is an effective method of acquiring data from topology and microstructure of surfaces. Basic concept of AFM is to measure forces between a sample surface and a sharp probing tip. The tip is mounted at the end of a cantilever connected to a piezoelectric actuator, which acts as a force sensor. Forces between the sample surface and probing tip differ as a function of distance. Measured force is used together with the information of the lateral location of the probing tip to form a topography image of the sample. Typically, the tip's length is below 5 μm and the diameter of apex is less than 10 nm while the cantilever's length is 100-500 μm. Restriction of AFM is that details smaller than the aspect ratio of the probing tip cannot be measured.

AFM has different operation modes, but in this project, only tapping mode was used. In tapping mode, the surface of the sample is mapped by lightly tapping it with an oscillating tip. Oscillation amplitude of the cantilever changes with surface topography. Changes in amplitude are measured with a laser beam that is reflected from the cantilever to a location sensitive light detector, as shown in Fig. 7 [23, 24].
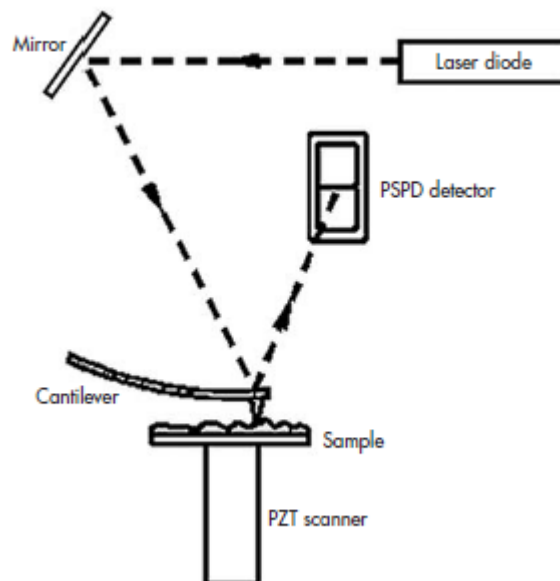

Figure 7. Principle of AFM measurement.

4.2. X-ray Diffraction

In X-ray diffraction (XRD), crystal structure of the sample is examined by measuring the intensity of scattered X-ray beam by using a diffractometer with two axes of independent rotation. X-ray source and detector are attached to the axes and a sample

holder is in the middle, as illustrated in Fig. 8 [25]. This setup enables measuring the intensity as function of angle 2θ.
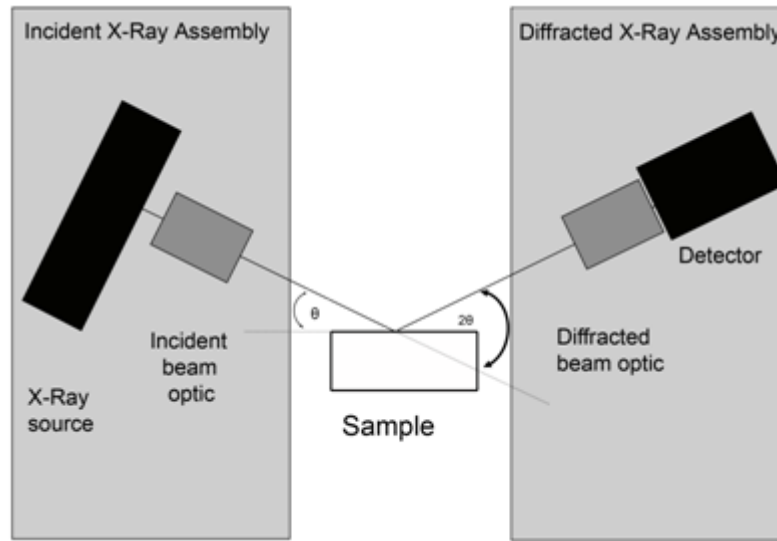

Figure 8. The XRD measurement setup.

In crystals, where all atoms are placed in a regular periodic array, i.e. lattice, diffracted beam of significant intensity can only be detected according to Bragg law, when:

$$2d \sin \theta = l\lambda \qquad (6)$$

where d is distance between diffraction planes, θ is angle between the radiation and the diffracting plane, l is order of reflection, and λ is wavelength of the radiation. Thus, the Bravais lattice constants can be obtained when monochromatic X-ray radiation is used [26].

Diffraction by either symmetrical- or asymmetrical-reflections can be obtained. In symmetrical-reflection θ-2θ measurement, diffracted X-rays from crystal lattice planes parallel to the surface are observed, as seen in leftmost image of Fig. 8. In symmetrical measurement, the incident and the diffracted angles against the sample surface plane are kept equal and usually have a range of several to tens of degrees. This results penetration of up to tens of μm by the incident X-ray beam, and because thin-films have commonly thickness of below 1 μm, strong diffraction from the substrate occurs [27].

Asymmetrical-reflection, or grazing incidence diffraction (GID), is shown in rightmost image of Fig. 9 [26]. The measurement is done under a specific diffraction geometry where the incident angle α is kept constant and usually in several degrees or less, while the detector on 2θ axis is rotated. In GID, the X-ray penetration depth can be controlled and kept within a thin-film.
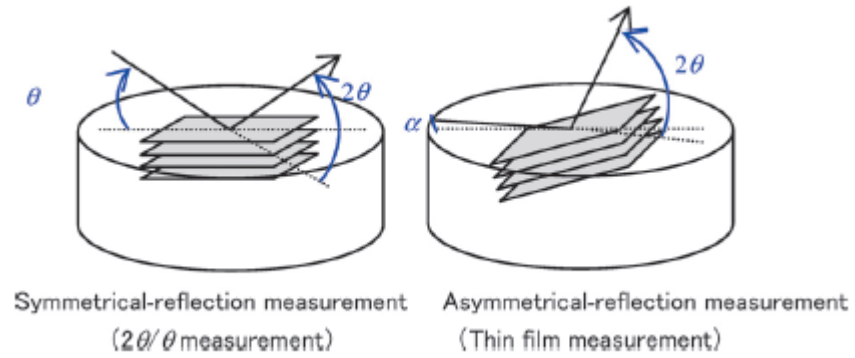
Figure 9. Principles of symmetrical-reflection and asymmetrical-reflection measurement configuration.

4.3. Raman Spectroscopy

In Raman spectroscopy, the sample is measured using monochromatic radiation, usually in visible spectrum. Most of the radiation Rayleigh scatters from the sample, but a minor part collides in inelastic way with the molecules of the sample. In Raman scattering, the energy of the photon is changed as it interacts with the molecular vibrations, phonons, or other excitations in the system by either absorbing, i.e. anti-Stokes Raman scattering, or loosing energy, i.e. Stokes Raman scattering. Energy of the Raman scattered photons is measured to calculate the energy shift between incoming and scattered photons. From this information, the intensity of Raman scattering as a function of inverse wavelength can be calculated [28].

5. EXPERIMENTAL

5.1. Pulsed Laser Deposition and Post-annealing Process

A pulsed XeCl-excimer laser (Lambda Physics COMPex 201) with wavelength of 308 nm and fluence of 0.88, 1.2, and 2 J/cm² were used for sample preparation. Deposition was done with 1800 pulses using 5 Hz repetition rate and pulse duration of 25 ns. Pure ceramic WO_3 target with density of 6.98×10^3 kg/m³ was used in depositions of nanoparticle thin films with varying thicknesses on silicon substrates with layer of SiO_2 on top. The deposition was done at room temperature using background oxygen pressure of 0.08, 0.2, and 0.54 mbar. Angle of incidence of the laser beam was 45° and the substrate was placed parallel with the target at the distance of 7.5 cm. After deposition, a set of samples were post-annealed in ambient air at temperatures of 400, 500, and 600 °C for a period of 1 hour. A set of samples was also left as deposited.

5.2. Atomic Force Microscopy

Surface morphology of the samples was studied by AFM (Veeco Dimension 3100) in tapping mode with scanning area of 1 μm × 1 μm. For better understanding of the morphology, values of rms roughness parameter R_q, Power Spectral Densities (PSD), and 2-dimensional Fourier transformations (2D-FFT) were calculated from the AFM micrographs.

5.3. X-Ray Diffraction

Crystal structures of the samples were studied using XRD measurement (Bruker AXS D8 Discover) using CuK_α radiation with wavelength of 1.5418 Å. For GID measurements, integration time of 3 s and increment angle of 0.025° were used. For θ-2θ measurements, integration time of 10 s and increment angle of 0.01° were used.

5.4. Raman Spectroscopy

Raman spectroscope (Labram-HR 800) was used to study the crystal structure of the samples. The spectra were recorded using integration time of 30 s between wavenumbers from 50 to 1200 cm^{-1} using Argon-ion laser with wavelength of 488 nm.

5.5. Field Emission Scanning Electron Microscopy

Top view and cross-sections of the samples were studied by field emission scanning electron microscopy (FESEM) (Zeiss Sigma). Samples were chipped in order to image

the cross-sections. To achieve better conductivity for imaging, 3 nm of platinum was sputtered on the samples.

5.6. Gas Sensing Measurements

In gas sensing measurements, the voltage for sensor heater was produced with HP 6626A System DC Power Supply and the resistance was measured with HP 3458A Multimeter. Measurements were done in gas chamber (Linkam THMSE600 heating stage).

6. RESULTS AND DISCUSSION

6.1. Surface Morphology Analysis

The surface morphology of the samples were measured using AFM and the results are shown in Figs. 9-12. It can be clearly seen, that the surfaces of the films are porous and constructed of nanoparticles, which are mostly in size of 10 to 40 nm. Deposition parameters had huge effect on the surface roughness. Samples deposited using 0.88 J/cm² under 0.54 mbar pressure were mostly too rough to be measured using AFM having peak to valley heights of over 1 µm inside the measuring area of 1 µm². Surface roughness parameters (R_q) are presented in Table 2. The R_q values of samples deposited under 0.54 mbar pressure have additional variance due to small measurement area in comparison to dimensions of surface features.

Table 2. R_q values.

Fluence (J/cm²)	O_2 pressure (mbar)	Temperature (°C)		R_q (nm)	
		RT	400	500	600
0.88	0.08	5.90	6.06	6.24	11.4
0.88	0.2	64.5	48.5	102	57.1
0.88	0.54	-	-	139	-
1.2	0.08	6.04	4.3	7.34	6.61
1.2	0.2	38.0	16.3	31.6	18.5
1.2	0.54	75.8	98.2	92.7	-
2	0.08	4.54	4.43	3.71	11.4
2	0.2	17.3	19.1	42.6	57.1
2	0.54	55.3	92.5	107	-

Micrographs from as-deposited samples are shown in Fig. 10. In (c) and (f), the surface consist of nanoparticles that have not formed distinctly separate agglomerates, but in micrograph (a), formation of agglomerates approximately consisting of only a few dozen nanoparticles can be seen. In all three samples, majority of the nanoparticles have diameter from 10 to 20 nm and the peak to valley depth is less than 50 nm.

In samples (b), (d), and (g), the background pressure during PLD was higher and the agglomerates are larger by a few magnitudes compared to those in (a). The size of the agglomerates and the peak to valley depth decreases as the fluence increases. According to micrograph (g), the nanoparticles are in same size as in (a), (c) and (f), but the size cannot be determined from (b) and (d), because the surface was too rough to observe small details. The micrographs (e) and (h) verify the impact of increasing pressure during PLD as the agglomerates have become even larger.

The correlation between PLD parameters and surface morphology of the sample is evident. Laser fluence and background pressure determine the energy of the plasma as explained in pages 10-11. The agglomeration starts as the energy of the plasma is low enough and as the energy gets lower, the agglomerates grow in size. However, it seems that the size of the nanoparticles does not change, but the number of nanoparticles per agglomerate increases.
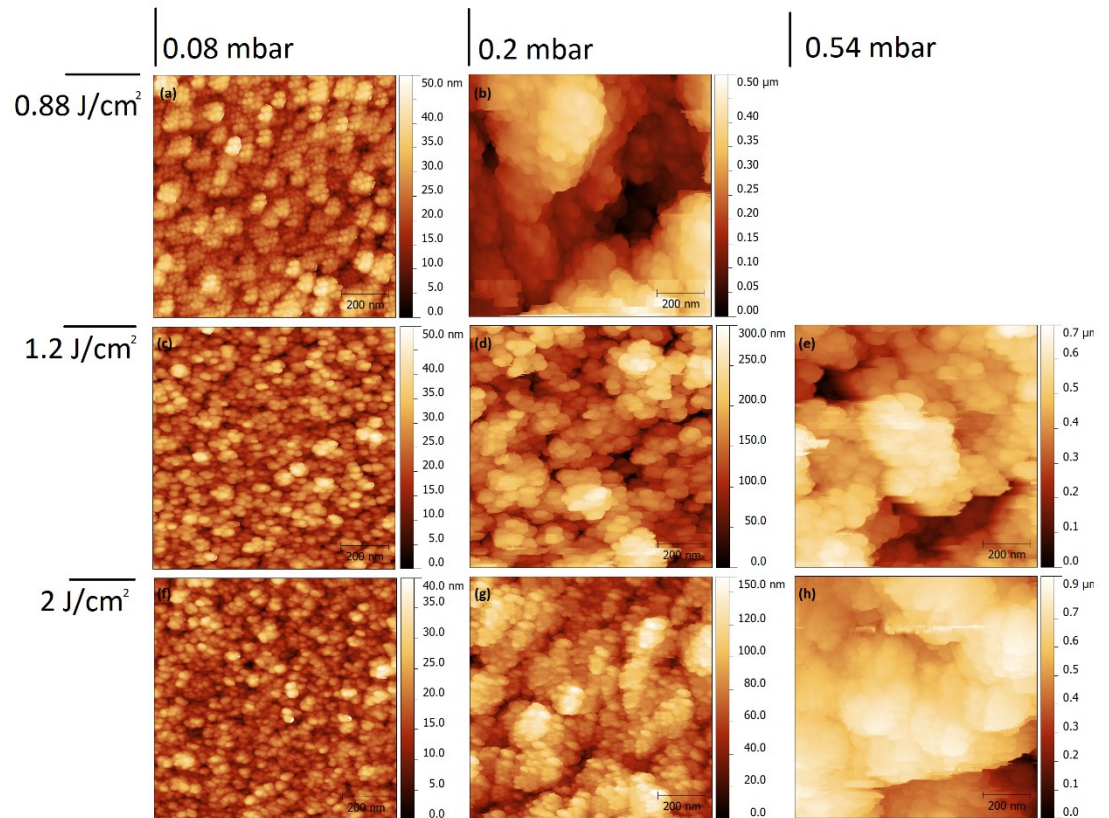
Figure 10. AFM micrographs of the as-deposited samples. Used fluence was 0.88 J/cm² under (a) 0.08 mbar, and (b) 0.2 mbar background pressure; 1.2 J/cm² under (c) 0.08 mbar, (d) 0.2 mbar, and (e) 0.54 mbar background pressure; 2 J/cm² under (f) 0.08 mbar, (g) 0.2 mbar, and (h) 0.54 mbar background pressure.

In Fig. 11, same dependency on fluence and pressure can be seen. Post-annealing at 400 °C has not had effect on size of the nanoparticles, but the agglomerates have shrunk, which can be seen from the R_q values, as well. This can be explained by the changes of bonds between nanoparticles. As the agglomerates are formed in the plasma plume, the nanoparticles form weak van der Waals bonds. During post-annealing at 400 °C the nanoparticles are sintered together and the stronger bonds make the agglomerates denser and thus smaller in size.
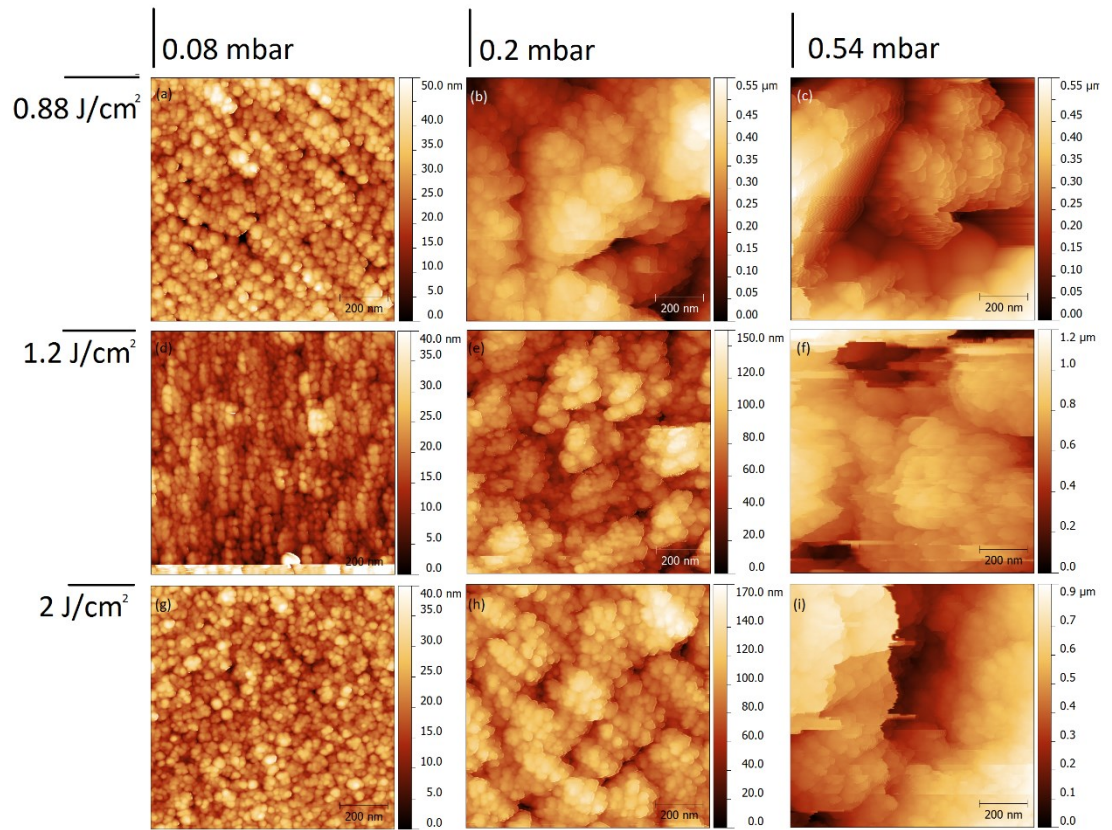
Figure 11. AFM micrographs of the samples annealed at 400 °C. Used fluence was 0.88 J/cm² under (a) 0.08 mbar, (b) 0.2 mbar, and (c) 0.54 mbar background pressure; 1.2 J/cm² under (d) 0.08 mbar, (e) 0.2 mbar, and (f) 0.54 mbar background pressure; 2 J/cm² under (g) 0.08 mbar, (h) 0.2 mbar, and (i) 0.54 mbar background pressure.

AFM micrographs of samples heated at 500 °C are shown in Fig. 12. Effects of thermal diffusion and Ostwald ripening can be seen in the surface morphology as the size of the nanoparticles has increased. The R_q values are mostly higher than in 400 °C, because porous material has merged in causing deep and narrow grooves between agglomerates. In sample (c), bare surface of the substrate can be seen with several separate agglomerates on it. Probably the agglomerates have tightened and shrunk during the post-annealing and the gaps between them have grown deep enough to reveal the surface of the substrate.
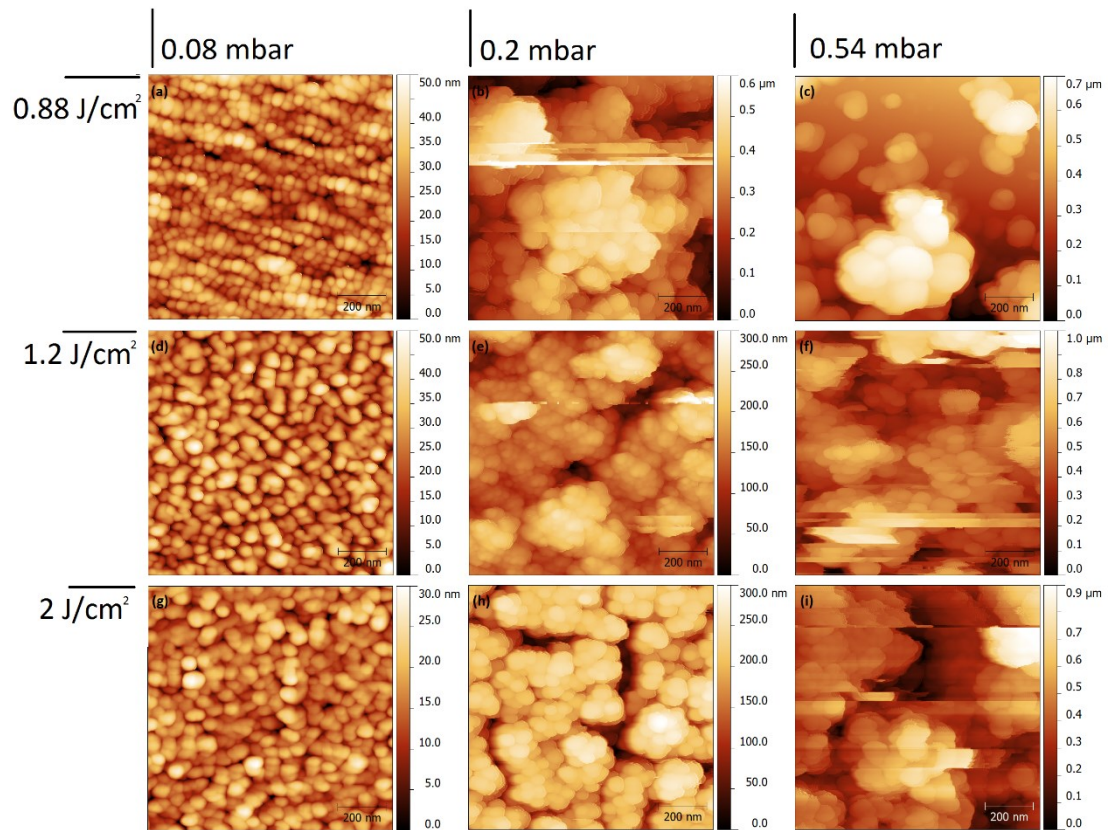
Figure 12. AFM micrographs of the samples annealed at 500 °C. Used fluence was 0.88 J/cm² under (a) 0.08 mbar, (b) 0.2 mbar, and (c) 0.54 mbar background pressure; 1.2 J/cm² under (d) 0.08 mbar, (e) 0.2 mbar, and (f) 0.54 mbar background pressure; 2 J/cm² under (g) 0.08 mbar, (h) 0.2 mbar, and (i) 0.54 mbar background pressure.

The effects of post-annealing at 600 °C are shown in Fig. 13. The surface morphology in samples deposited under pressure of 0.08 mbar has been re-shaped heavily by thermal diffusion. The nanoparticles have roughly doubled or tripled in size and distinct islands with different lateral orientations have been formed, which can be seen especially in micrograph (a). In samples deposited under 0.2 mbar, the size of the nanoparticles has grown and the peak to valley depth has decreased, but otherwise the surface structure appears to be similar with those in Fig. 12.
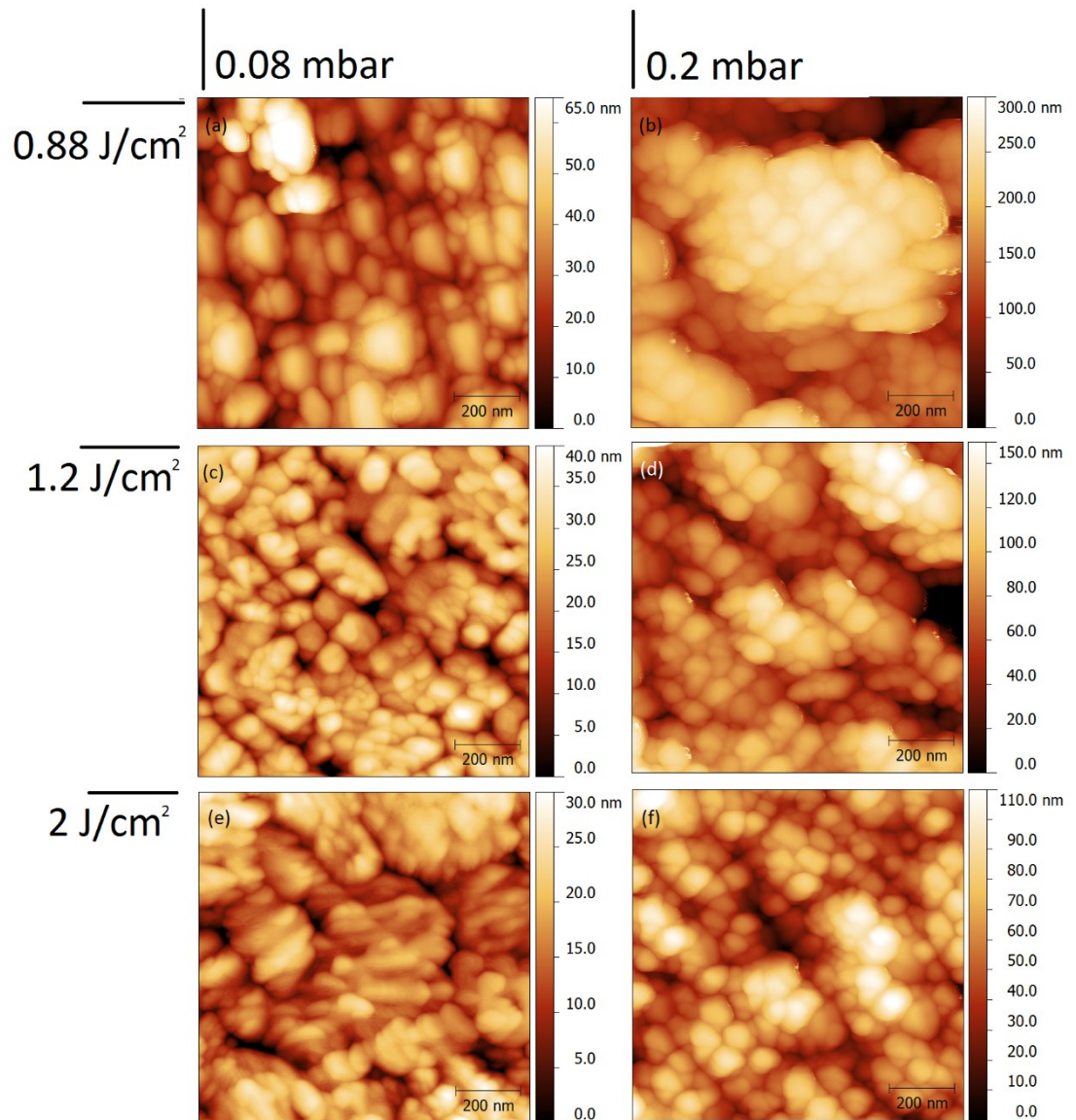
Figure 13. AFM micrographs of the samples annealed at 600 °C. Used fluence was 0.88 J/cm² under (a) 0.08 mbar and (b) 0.2 mbar background pressure; 1.2 J/cm² under (c) 0.08 mbar and (d) 0.2 mbar background pressure; 2 J/cm² under (e) 0.08 mbar and (f) 0.2 mbar background pressure.

Lateral orientation can be seen in some of the films, especially in Fig. 11 (a) and (d). This is likely to be only a regional attribute of the surface that is seen because of heterogeneous nature of the films and small scanning area of the AFM. The FESEM analysis, that is covered subsequently, strengthened this theory as larger scanning areas did not have signs of lateral orientation.

The particle sizes of the agglomerates were analyzed from the AFM micrographs. Fig. 14 demonstrates the behavior of samples deposited under background pressure of 0.08 mbar using fluence of 0.88 J/cm². The analysis shows very clearly that the agglomerates first indeed shrink during post-annealing, but grow larger at higher temperatures.
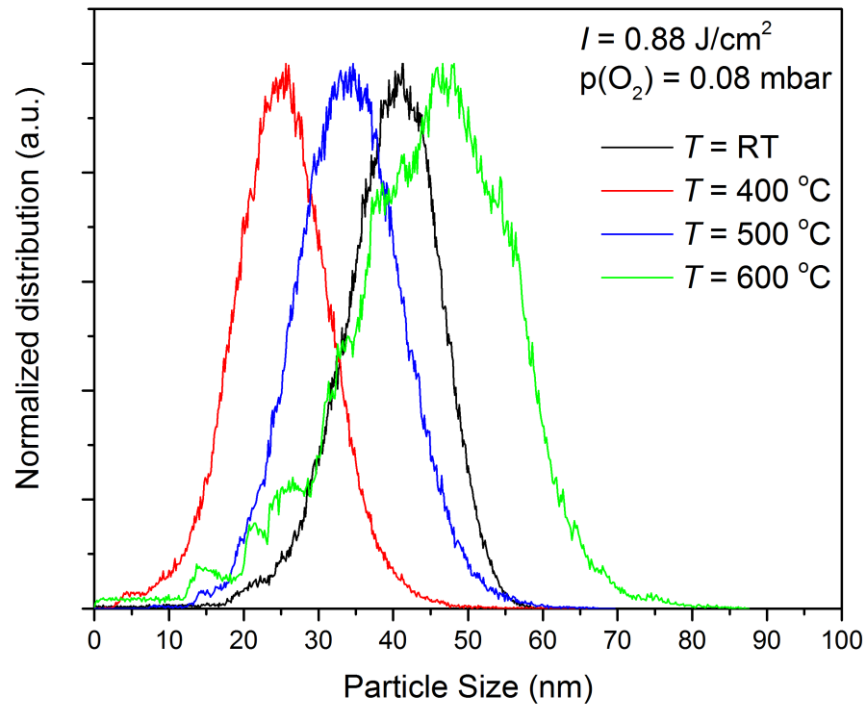
Figure 14. Particle size distributions of the agglomerates.

6.1.1. Power Spectral Densities

Power spectral densities (PSD) were calculated from AFM micrographs [29]. Micrographs from samples deposited in 0.54 mbar had too much artifacts for reliable calculations, therefore only data from samples deposited in 0.08 mbar and 0.2 mbar was used.

Figs. 15-17 show that despite of fluence, the curves for both pressures divide into two separate groups. Samples post-annealed in 600 °C deviate from these groups because of the major surface morphological changes, as was seen from the AFM micrographs. The tendency of fluence can be seen, especially in the 0.08 mbar curves, where the visible maximum moves to greater spatial frequency as a function of increasing post-annealing temperature, which indicates of smaller structure. Same tendency can be found in the samples deposited under pressure of 0.2 mbar. This verifies that pressure and fluence have opposite effects on surface roughness, but the effect of pressure is more dominate, and also that post-annealing below 600 °C does not have major impact on the surface roughness.
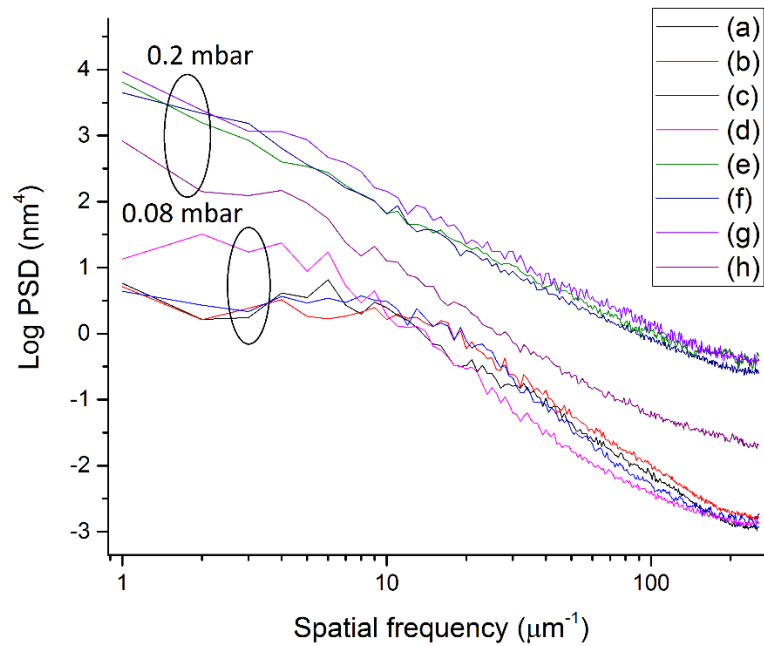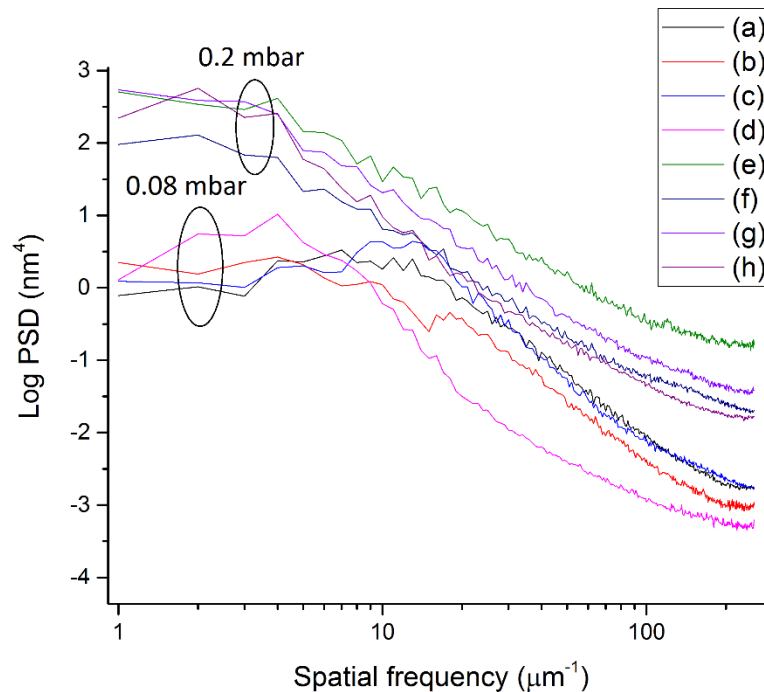
Figure 15. PSD curves of samples deposited using 0.88 J/cm² laser fluence. Background pressure was 0.08 mbar with post-annealing of (a) room temperature, (b) 400 °C, (c) 500 °C, (d) 600 °C, and 0.2 mbar with post annealing of (e) room temperature, (f) 400 °C, (g) 500 °C, and (h) 600 °C.

Figure 16. PSD curves of samples deposited using 1.2 J/cm² laser fluence. Background pressure was 0.08 mbar with post-annealing of (a) room temperature, (b) 400 °C, (c) 500 °C, (d) 600 °C, and 0.2 mbar with post annealing of (e) room temperature, (f) 400 °C, (g) 500 °C, and (h) 600 °C.
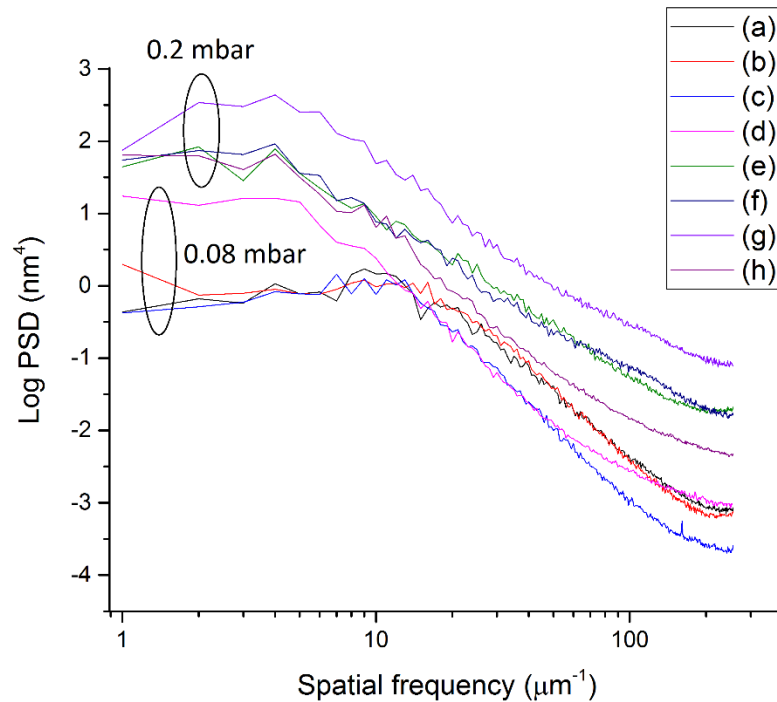
Figure 17. PSD curves of samples deposited using 2 J/cm² laser fluence. Background pressure was 0.08 mbar with post-annealing of (a) room temperature, (b) 400 °C, (c) 500 °C, (d) 600 °C, and 0.2 mbar with post annealing of (e) room temperature, (f) 400 °C, (g) 500 °C, and (h) 600 °C.

6.1.2. 2D-FFT Created Scattering Field Images

Two-dimensional fast Fourier transformation (2D-FFT) was used to construct scattering field images from the AFM micrographs. Figs. 18-20 demonstrate the effects seen in the 2D-FFT data. Same phenomenon could also be observed in samples deposited under 0.54 mbar pressure, but because the AFM micrographs included lots of artifacts, the scattering field images are not presented here.

   In each figure, it can be seen that the scattering pattern in the as-deposited samples is not completely symmetrical, but becomes more circular shaped in post-annealing temperatures of 500 and 600 °C. This indicates that the surface morphology has weak lateral orientation after PLD process, but it fades out in thermal diffusion during post-annealing. Post-annealing also results in disappearance of smaller phases as the nanoparticles begin to grow in size. However, post-annealing at 400 °C seems to have only a minor effect on surface morphology, which was noted from AFM micrographs on pages 23-25, as well.

   Comparison of Figs. 18 and 19 reveals that the scattering pattern is more spread out in samples deposited using higher fluence, which can be explained by existence of smaller agglomerates caused by more energetic plasma during deposition process. Fig. 20 shows that the disappearance of smaller phases at higher annealing temperatures is reduced in samples deposited under higher pressure. The same tendency was noted

from the AFM micrographs, where surface morphology was affected less by post-annealing on samples, which were deposited under higher pressure.
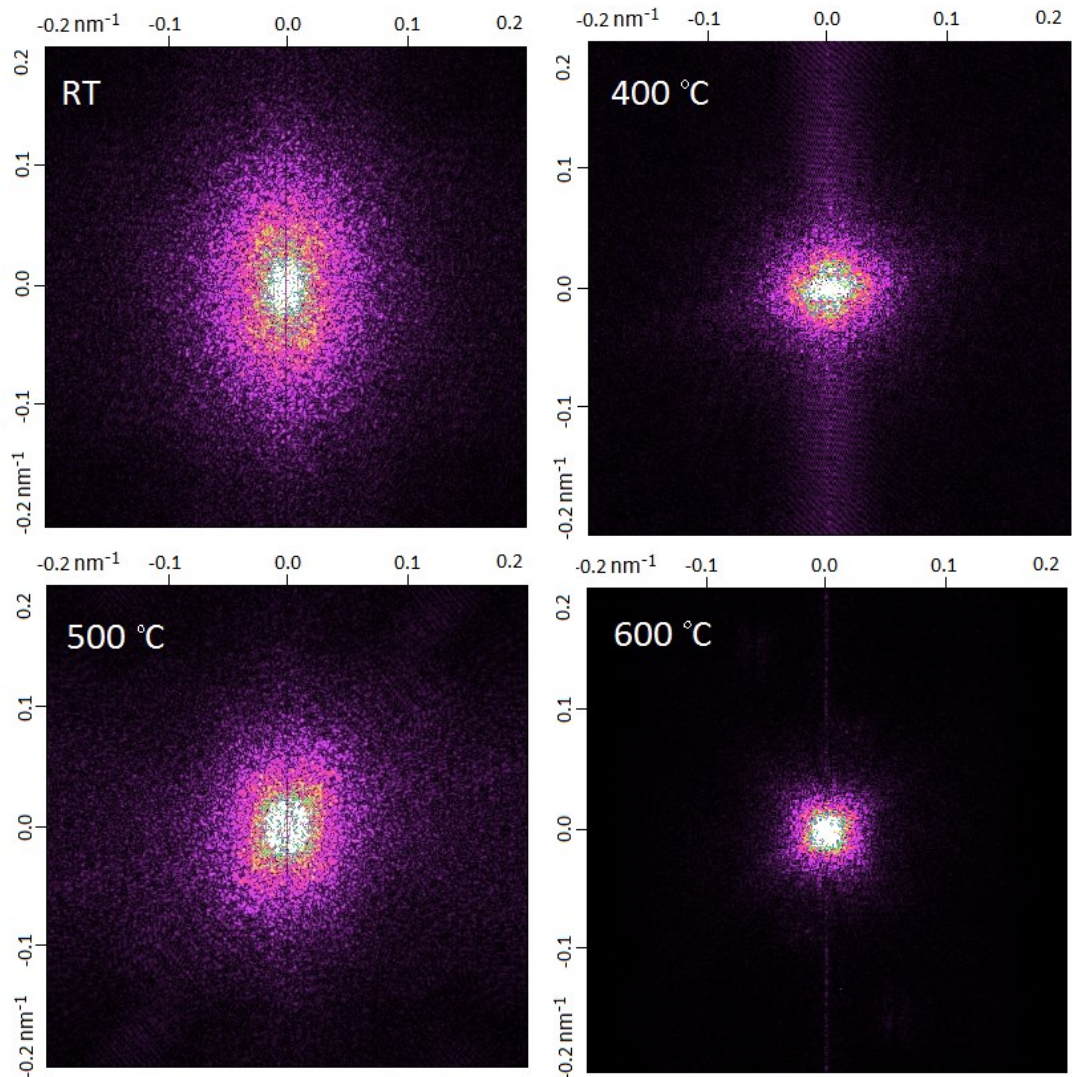

Figure 18. Scattering field images of samples with different post-annealing temperatures deposited under 0.08 mbar pressure using fluence of 1.2 J/cm².
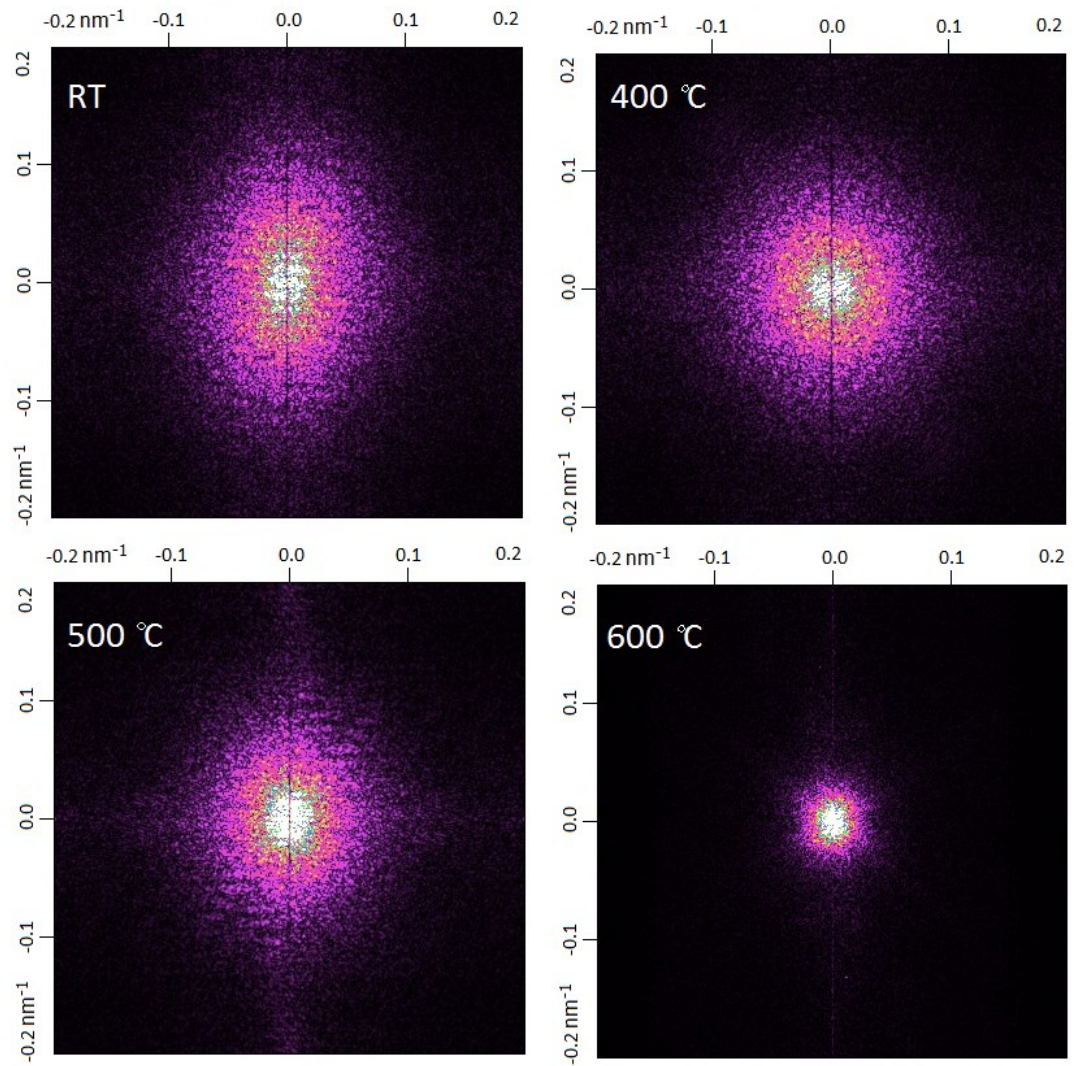
Figure 19. Scattering field images of samples with different post-annealing temperatures deposited under 0.08 mbar pressure using fluence of 2 J/cm².
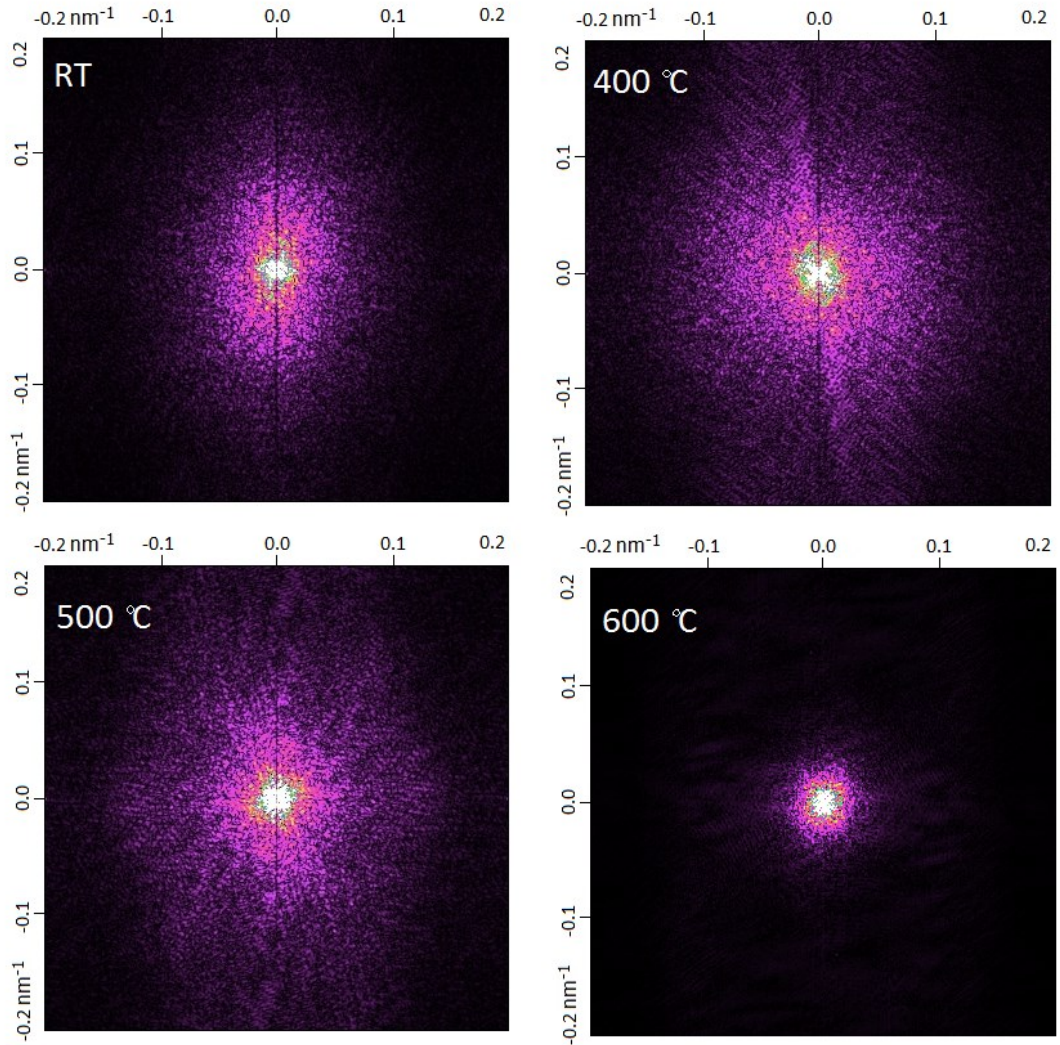
Figure 20. Scattering field images of samples with different post-annealing temperatures deposited under 0.2 mbar pressure using fluence of 2 J/cm².

6.2. X-Ray Diffraction

6.2.1. Asymmetrical-reflection Measurements

Effects of fluence, background pressure, and post-annealing temperature on crystal structure of WO_3 samples were measured using GID. Data from as-deposited samples is shown in Fig. 21, and it can be noticed that no significant peaks can are formed, which indicates that most of the crystallization process occurs during post-annealing. Figs. 22-24 verify that post-annealing enables crystallization, as well as the grain growth, and the effects of fluence and pressure can be observed. The strongest peaks were found between 22° and 25°. The second interesting area was between 32° and 35°. Diffraction peaks for ε- and γ-phases are labeled on the horizontal axis according to Woodward and Salje [30, 31]. The triclinic δ-phase did not fit into the peaks in measured data.
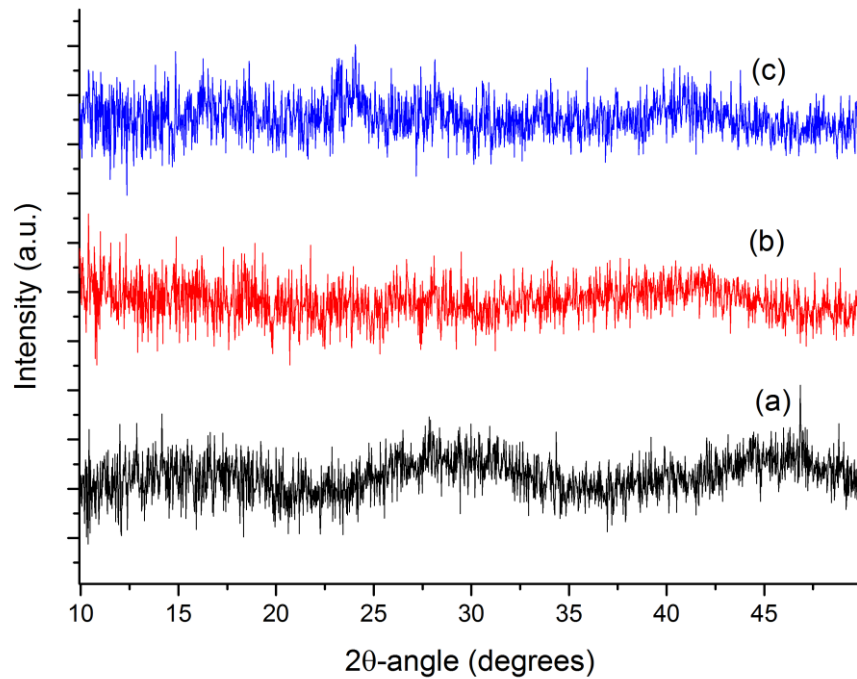
Figure 21. X-ray GID patterns of as-deposited samples using 1.2 J/cm² fluence under (a) 0.08 mbar, (b) 0.2 mbar, and (c) 0.54 mbar background pressure. Background radiation has been removed from the data.

In Fig. 22, curves (d) and (g) show that only γ-phase with strong orientation is present, as the peaks at 24.25° and 34.1° are significantly higher than the others. The peaks at 23.15°, 23.60°, and 24.35° agree with the (002), (020), and (200) crystal planes of γ-phase, respectively [20]. In (a), the same orientation does not exist and the peak at 24.25° is broad, and can be explained with an additional peak at 24.1° that is caused by the ε-phase. The existence of ε-phase can also be noted from the area at 33°-34°, where (d) and (g) have one strong peak at 34.2°, and (a) has several peaks between 33° and 34.2°. Both ε- and γ-phases have peaks in those ranges, but it is unlikely that either alone could cause such broadening as seen in (a). When comparing (d) and (e) or (g) and (h), it can be seen that the ε-phase appears with higher processing pressure. As explained on pages 10-11, the fluence is directly and background pressure is inversely proportional to the energy of plasma during PLD process. Thus, it can be concluded that during the post-annealing caused crystallization process, mostly γ-phase with high orientation is formed in samples deposited with highly energetic plasma. With less energetic plasma, the γ-phase is less oriented and ε-phase is formed, as well. Also, oxygen deficiency and small grain size promote the formation of ε-phase.

Curves (b) and (f) show considerably weaker crystallization degree, as well as signs of amorphous phase, and (c) is mostly amorphous. Because these samples were created with least energetic plasma, it can be noted that deposition parameters have a significant effect on crystallization even though the process takes place mostly during the post-annealing. The reason for this is suspected to be that the thermal energy of post-annealing is consumed in sintering the agglomerates, as explained on pages 24-25, and thus there is not energy left for crystallization process.
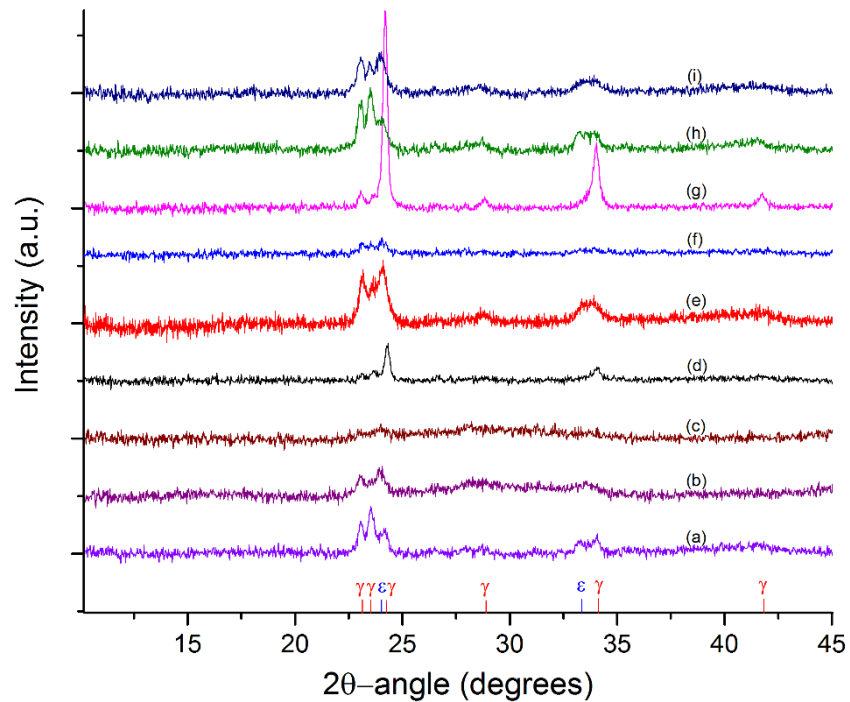
Figure 22. X-ray GID patterns of samples post-annealed at 400 °C. Used fluence was 0.88 J/cm² under (a) 0.08 mbar, (b) 0.2 mbar, and (c) 0.54 mbar background pressure; 1.2 J/cm² under (d) 0.08 mbar, (e) 0.2 mbar, and (f) 0.54 mbar background pressure; 2 J/cm² under (g) 0.08 mbar, (h) 0.2 mbar, and (i) 0.54 mbar pressure. Background function has been removed from the data. Curve (e) was measured using 10 s integration time, while others with 3 s..

The effect of annealing at 500 °C can be seen from Fig. 23. Curve (c) shows that 500 °C is enough for crystallization process to take place even in the presence of largest agglomerates in contrary to 400 °C. The orientation in (d) and (g) is very similar to that in Fig. 22, and so is the dependency between presence of ε- and γ-phases, and fluence and pressure. It is obvious that amount of ε-phase maximizes in the samples deposited with a low-energy plasma, i.e. with lower laser beam fluence and higher partial oxygen pressure, though the effect of fluence is minor compared to level of oxygen pressure.
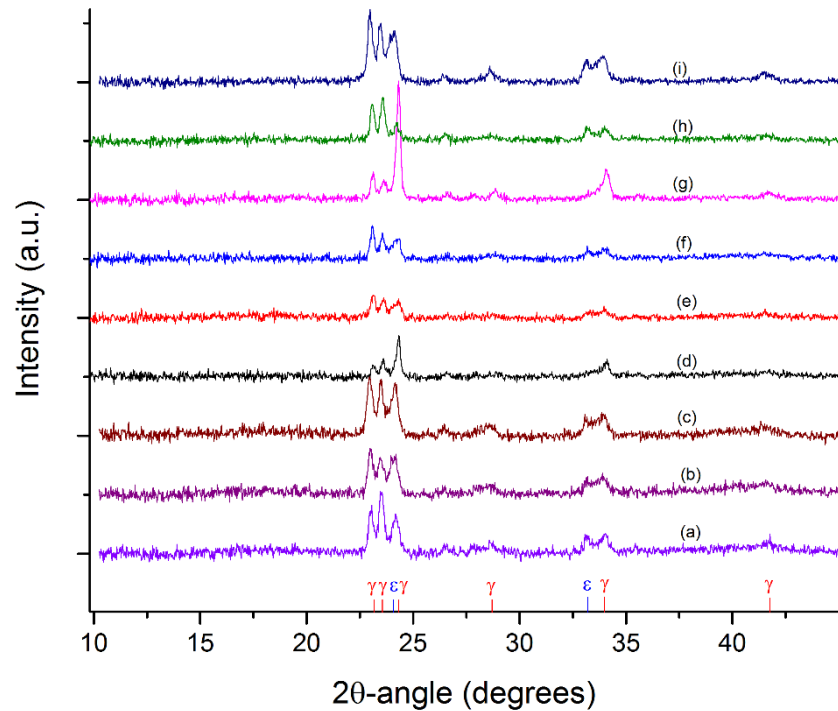
Figure 23. X-ray GID patterns of samples post-annealed at 500 °C. Used fluence was 0.88 J/cm² under (a) 0.08 mbar, (b) 0.2 mbar, and (c) 0.54 mbar background pressure; 1.2 J/cm² under (d) 0.08 mbar, (e) 0.2 mbar, and (f) 0.54 mbar background pressure; 2 J/cm² under (g) 0.08 mbar, (h) 0.2 mbar, and (i) 0.54 mbar pressure. Background function has been removed from the data.

Data from samples heated at 600 °C is shown in Fig. 24. The change from 500 °C is that implications of the ε-phase have disappeared completely, and new peaks have appeared at 11° and 21.8°. According to crystal structures of WO_3, no crystal planes should be found at around 11°, but the peak is possibly caused by the second coordination sphere of W—W distances in WO_6 octahedra [32]. The cause of peak found at 21.8° is unknown, but it could be caused by more uncommon W_xO_y compound formed at higher post-annealing temperature.
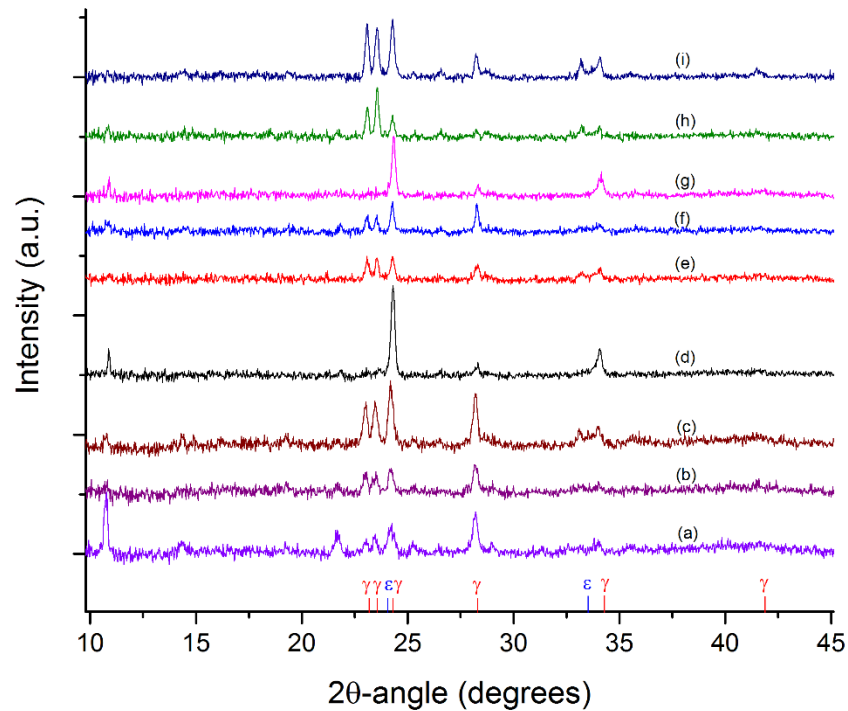
Figure 24. X-ray GID patterns of samples post-annealed at 600 °C. Used fluence was 0.88 J/cm² under (a) 0.08 mbar, (b) 0.2 mbar, and (c) 0.54 mbar background pressure; 1.2 J/cm² under (d) 0.08 mbar, (e) 0.2 mbar, and (f) 0.54 mbar background pressure; 2 J/cm² under (g) 0.08 mbar, (h) 0.2 mbar, and (i) 0.54 mbar pressure. Background function has been removed from the data.

6.2.2. Symmetrical-reflection Measurements

By analysing the data from GID measurements, array of samples were picked for θ-2θ measurements. The sharpest peak at 32.65° comes from silicon substrate, because in θ-2θ measurements the penetration depth of X-rays is greater than in GID as explained on page 19.

   Weak peaks from non-post-annealed samples were found, which proves that some crystallization takes place already in the plasma plume. The crystallization degree in plasma was found to be higher with higher background pressure, as seen in Fig. 25. This indicates that the crystallization process during deposition occurs in the early stages of PLD before the expansion of plasma. However, no signs of crystallization in the plasma plume could be found from the samples deposited in fluence of 0.88 J/cm².
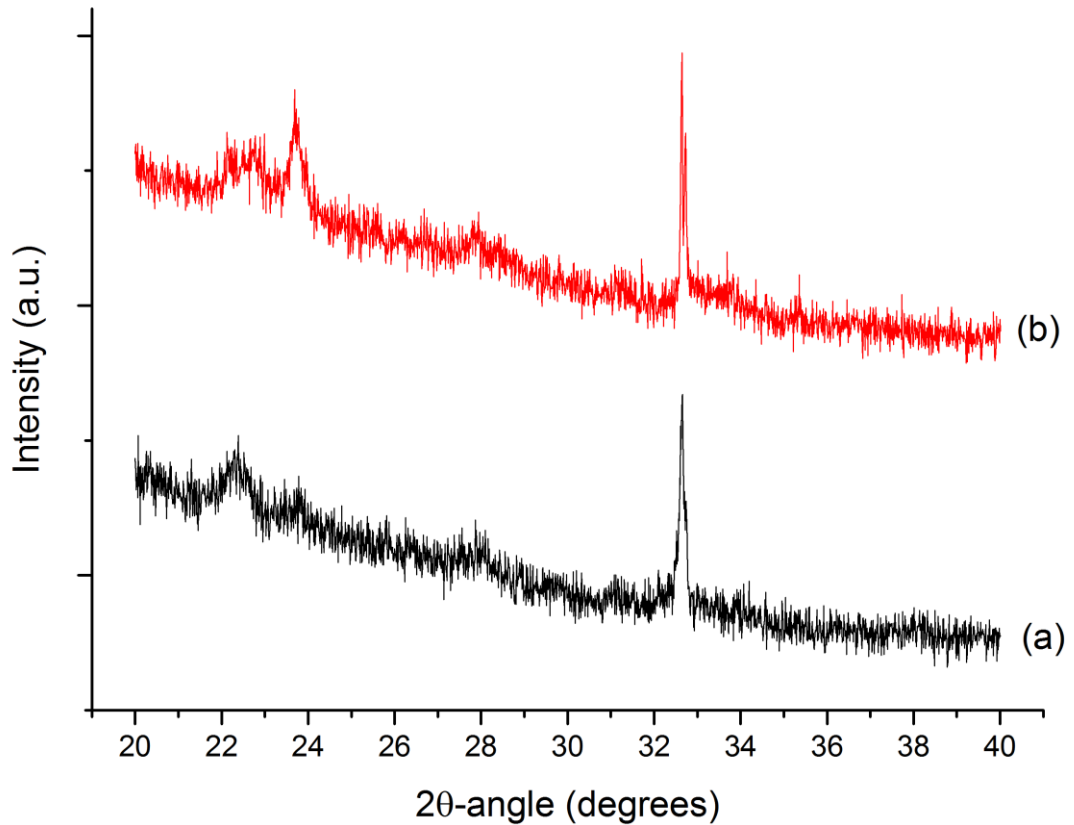
Figure 25. θ-2θ graphs of as-deposited samples deposited using 1.2 J/cm² fluence under background pressure of a) 0.08 mbar and b) 0.54 mbar.

There is no radical change in shape or relations of the peaks between GID and θ-2θ measurements, as seen in Fig. 26. But because of the longer integration time, signal to noise ratio is much better making it possible to analyze the data more properly. Rietveld analysis was done to θ-2θ data using Bruker's TOPAS software [33]. Results are shown in Table 3. According to Rietveld analysis, the phase changes in phase distribution are much lesser than those suspected from GID data. This could be caused by falsely interpreting different kind of orientation as different kind of phase distribution. It can also be noted that grain size in ε-phase is significantly smaller than that in γ-phase.
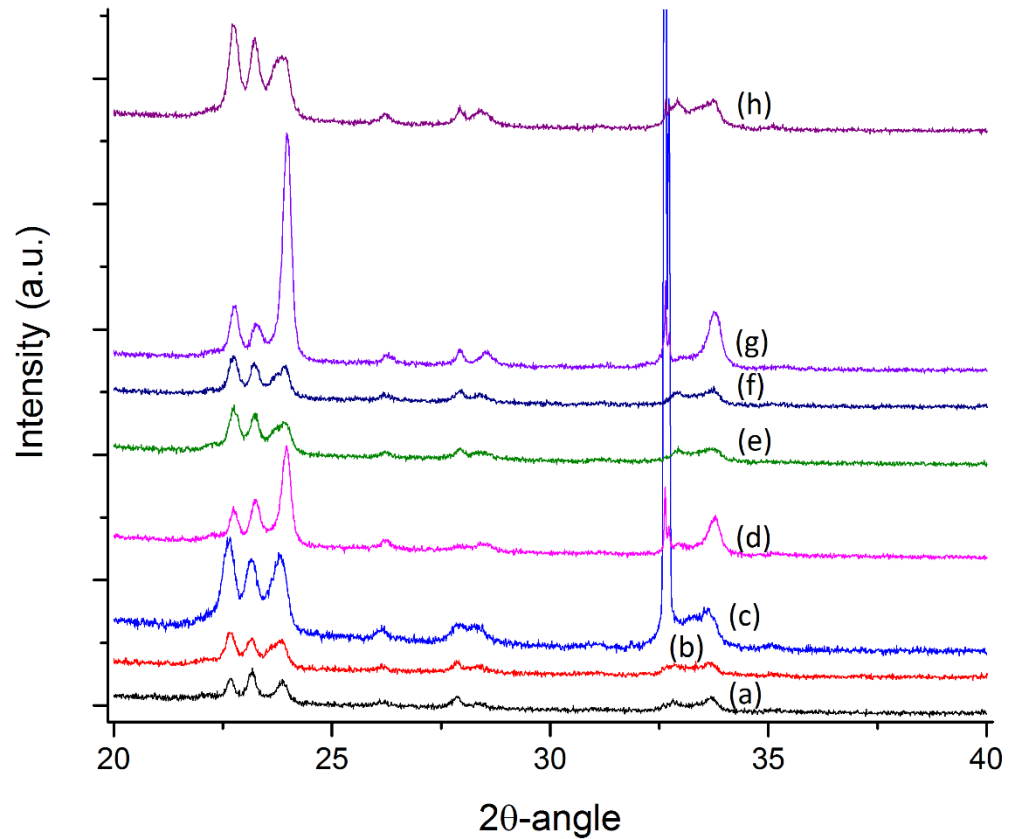
Figure 26. θ-2θ patterns of samples post-annealed at 500 °C deposited using 0.88 J/cm² fluence under background pressure of a) 0.08 mbar, b) 0.2 mbar, c) 0.54 mbar; 1.2 J/cm² fluence under background pressure of d) 0.08 mbar, e) 0.2 mbar, f) 0.54 mbar; 2 J/cm² fluence under background pressure of g) 0.08 mbar and h) 0.54 mbar.

Table 3. Phase distributions and grain sizes according to Rietveld analysis made from θ-2θ data. All samples were post-annealed at 500 °C.

Fluence (J/cm²)	O$_2$ pressure (mbar)	Percentage of γ-phase	Grain size of γ-phase (nm)	Percentage of ε-phase	Grain size of ε-phase (nm)
0.88	0.08	75 %	43.6	25 %	25.3
0.88	0.2	63 %	31.9	37 %	16.2
0.88	0.54	77 %	22.2	23 %	17.5
1.2	0.08	65 %	44.5	35 %	26.7
1.2	0.2	77 %	28.4	23 %	22.2
1.2	0.54	72 %	33.9	28 %	20.1
2	0.08	73 %	42.8	27 %	22.2
2	0.54	79 %	27.0	21 %	26.1

Grain size distributions were also calculated by Warren-Averbach, Scherrer, and integral breath methods [26, 34, 35]. Scherrer method gave grain sizes of over 100 nm, and from AFM micrographs it was seen that the size of the nanoparticles were almost a decade smaller. Warren-Averbach and integral breath methods gave more reliable data from the θ-2θ measurements.

WinFit program was used for calculations with Cauchy function [36]. Due to the small size of the samples, most of the peaks were too weak to be used, and due the nature of WO$_3$ most of the peaks overlap a lot. Because of this, only the peaks at 22° to 25° were used in fitting simulation. Thus, the sequential reflections could not be used which adds some error to the absolute value of the results, but the results should be comparable with each other. Because the strong presence of amorphous phase in non-post-annealed samples, grain size distribution was calculated only for post-annealed samples. The peak values of the grain size distributions of γ-phase are shown in Table 4.

Table 4. Average grain sizes according to Warren-Averbach method.

PLD processing parameters		Average grain size (nm)		
Fluence (J/cm²)	O$_2$ pressure (mbar)	T=400 °C	T=500 °C	T=600 °C
0.88	0.08	10	14	21
0.88	0.2	-	12	14
0.88	0.54	-	13	26
1.2	0.08	11	13	15
1.2	0.2	-	14	15
1.2	0.54	-	13	26

The Figs. 27 and 28 show examples of fitting results. Because only one significant peak for ε-phase was found, reliable grain size distribution could not be calculated. The grain size distribution of γ-phase varied from 11 to 26 nm. Increase of annealing temperature was found to grow the size of the grains. Fluence or background pressure did not have noticeable effect on the samples heated in 400 °C or 500 °C, but for 600 °C, the samples with larger agglomerates had larger grains. Values are much smaller than those acquired by Rietveld method, which might be due to the small amount of peaks used in calculations. Also the tendency of decreasing grain size as a function of background pressure cannot be seen in Warren-Averbach data. Any dependency on fluence cannot be seen in either data.
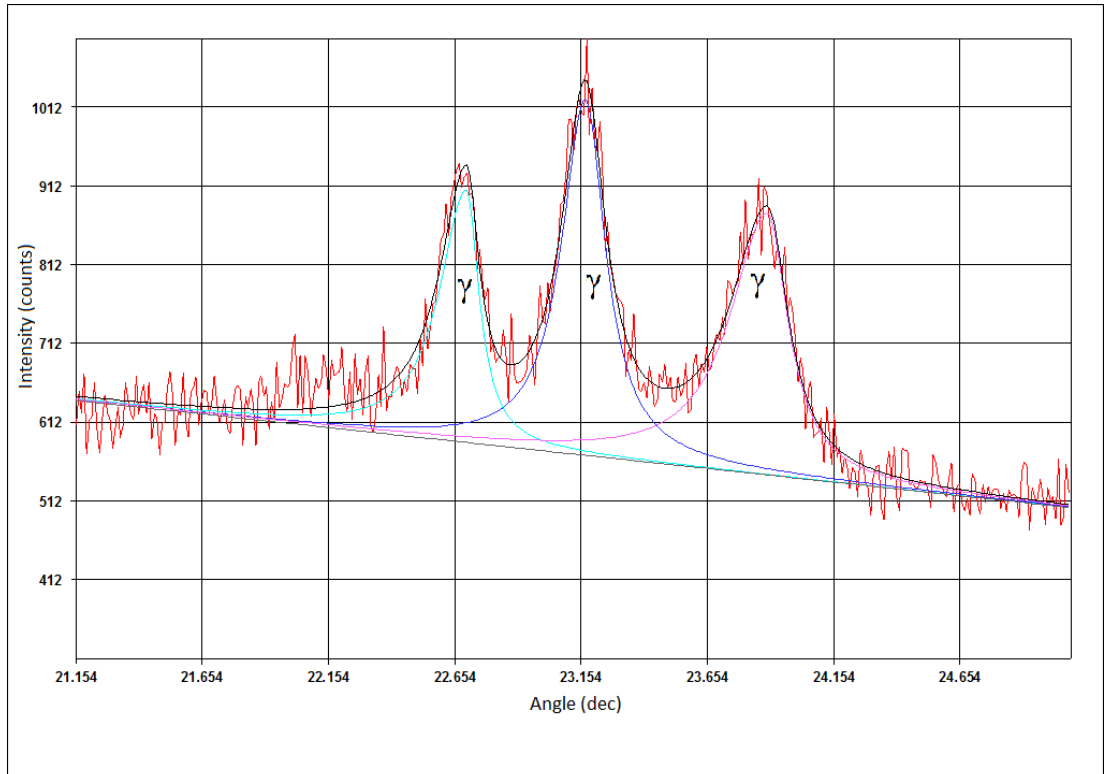
Figure 27. Result of fitting process of sample with γ-phase deposited under 0.08 mbar pressure using fluence of 0.88 J/cm² and post-annealed in 500 °C.
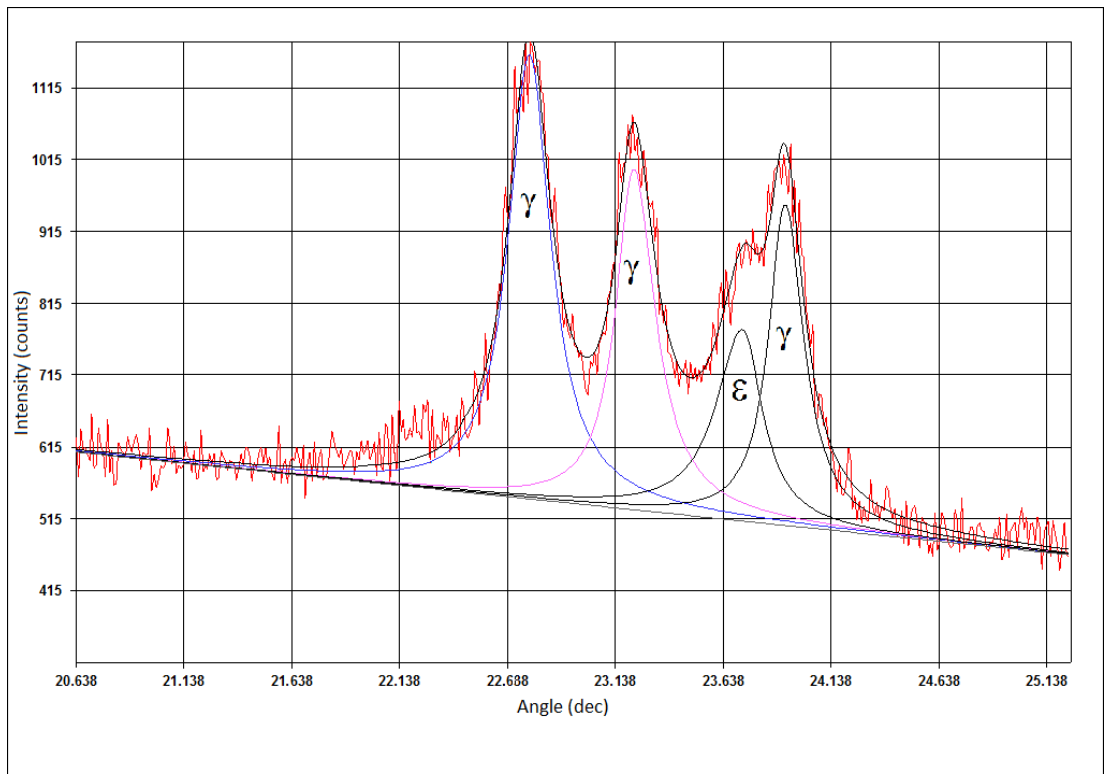

Figure 28. Result of fitting process of sample with ε- and γ-phases deposited under 0.54 mbar pressure using fluence of 1.2 J/cm² and post-annealed in 500 °C.

6.3. Raman Spectroscopy

Raman spectra for each sample are shown in Figs. 29-32, in which phases are identified and labeled according to Souza Filho and Cazanelli [37, 38]. The peak at 820 cm^{-1} fits for both ε- and γ-phase.

From Fig. 29 it can be seen that (a), (d), and (g) are mostly amorphous, but signs of crystallization can be seen in (b), (c), (e), and (h) and especially in (f) and (i). It seems that the crystallization process during PLD at room temperature requires both high fluence and high background pressure. Same tendency was found in Fig. 25, but unlike in XRD measurements, weak signs of crystallization can be seen in Raman data even in samples deposited with the lowest fluence. The phase distribution is more ε-phase oriented, which indicates that either ε-phase crystallizes more easily or phase transition to γ-phase occurs in heat treatment.
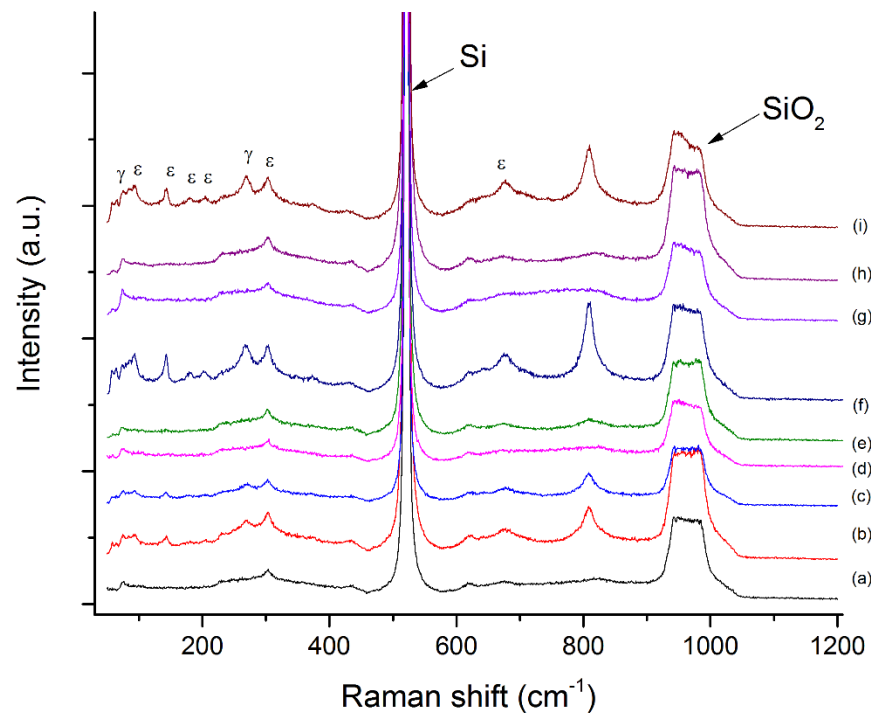

Figure 29. Raman spectra of as-deposited samples. Used fluence was 0.88 J/cm² under (a) 0.08 mbar, (b) 0.2 mbar, and (c) 0.54 mbar background pressure; 1.2 J/cm² under (d) 0.08 mbar, (e) 0.2 mbar, and (f) 0.54 mbar background pressure; 2 J/cm² under (g) 0.08 mbar, (h) 0.2 mbar, and (i) 0.54 mbar background pressure.

From Fig. 30 (a), (d), and (g), it can be seen that samples created in lowest pressure consist of mostly γ-phase. With higher pressure, the ε-phase appears in addition. This can be seen especially from the second peaks at 95 and 147 cm^{-1}, the two peaks at 182 and 202 cm^{-1} and from the broadening of the peak at 715cm^{-1}. The peaks at around 715 cm^{-1} are also typical for several phases of crystalline WO$_3$ and correspond to the symmetric and asymmetric O—W—O stretching modes [20]. The effect of fluence is

opposite, but less significant. It can be seen especially from curve (h), where the ε-phase is noticeable weaker than in curves (b) or (e).
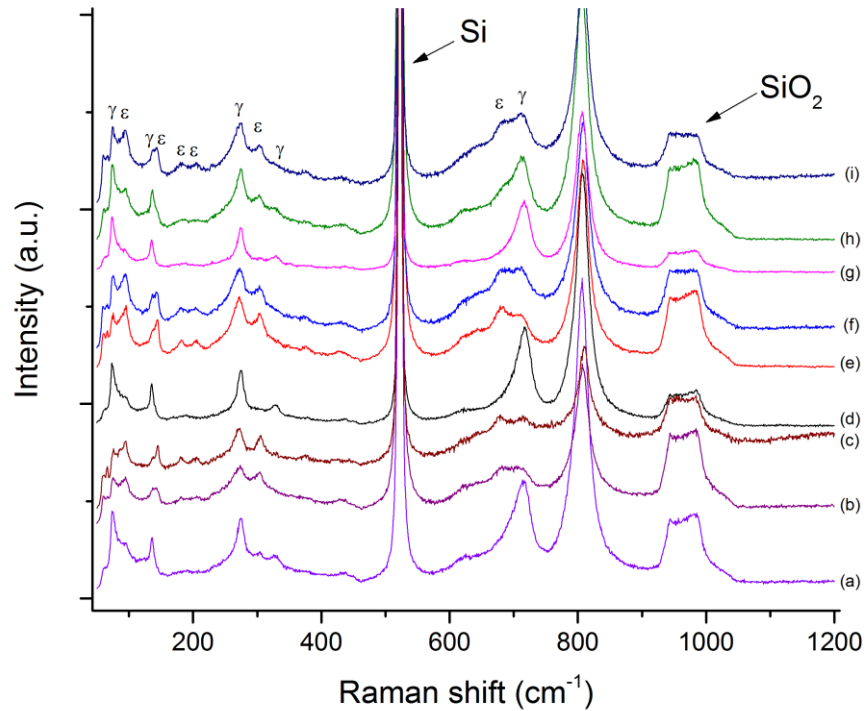

Figure 30. Raman spectra of samples post-annealed at 400 °C. Used fluence was 0.88 J/cm² under (a) 0.08 mbar, (b) 0.2 mbar, and (c) 0.54 mbar background pressure; 1.2 J/cm² under (d) 0.08 mbar, (e) 0.2 mbar, and (f) 0.54 mbar background pressure; 2 J/cm² under (g) 0.08 mbar, (h) 0.2 mbar, and (i) 0.54 mbar background pressure.

In Fig. 31, the samples are more γ-phase oriented. The ε-phase is present, but it is clearly weaker than in Fig. 30. It also appears that crystallization degree has increased, since the area at 685 cm^{-1} has distinct peaks compared to Fig. 29.

Figure 31. Raman spectra of samples post-annealed at 500 °C. Used fluence was 0.88 J/cm² under (a) 0.08 mbar, (b) 0.2 mbar, and (c) 0.54 mbar background pressure; 1.2 J/cm² under (d) 0.08 mbar, (e) 0.2 mbar, and (f) 0.54 mbar background pressure; 2 J/cm² under (g) 0.08 mbar, (h) 0.2 mbar, and (i) 0.54 mbar background pressure.

In Fig. 32, the ε-phase has mostly disappeared. The peaks of γ-phase are sharper and higher, which indicates higher orientation and more complete crystal structure. In curves (a), (c), and (f) new peaks have appeared at 860 and 885 cm^{-1}, as well as a peak at 955 cm^{-1}, which can also be found in (e) and (i). The peak at 955 cm^{-1} agrees with W^{6+}=O stretching mode of terminal oxygen atoms that are likely located at the surface of the nanoparticles [39, 40]. This peak is related with the nanostructure, but it is not present in the other curves. Since all the samples consist of nanoparticles, the reason for absence of the peak at 955 cm^{-1} could be in the heterogeneous structure of the films, and very small measuring area of the Raman spectroscopy. The peaks at 860 and 885 cm^{-1} do not suit with plain WO_3, Si, or SiO_2, but could be caused by W─O─W vibrations of W_3O_9 [41].
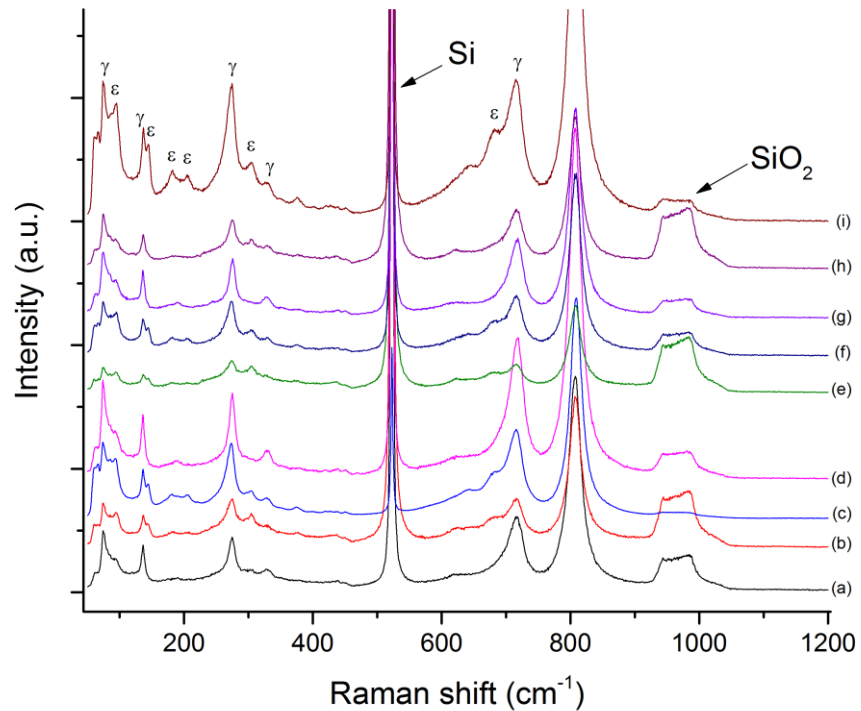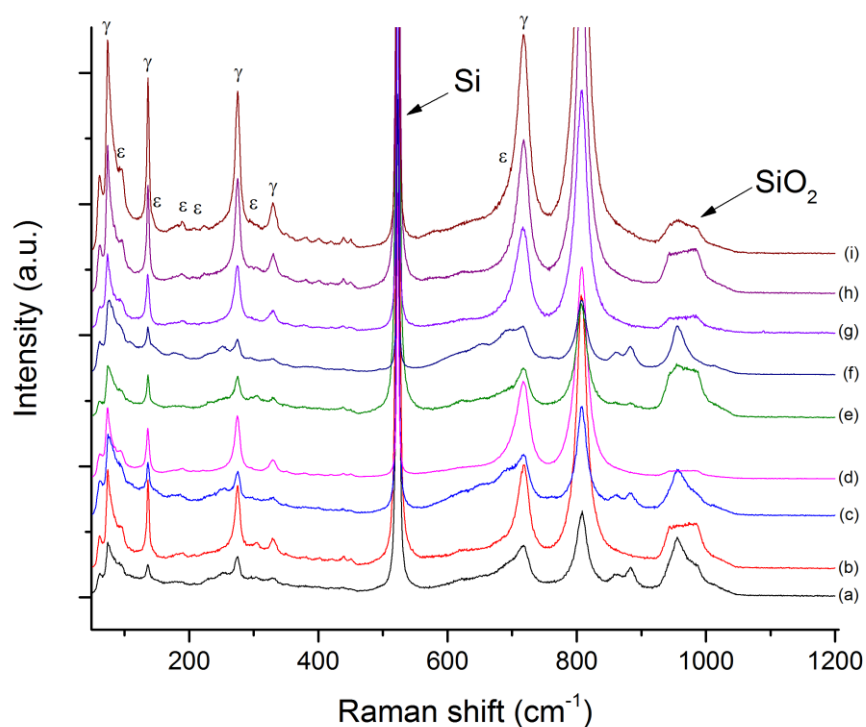
Figure 32. Raman spectra of samples post-annealed at 600 °C. Used fluence was 0.88 J/cm² under (a) 0.08 mbar, (b) 0.2 mbar, and (c) 0.54 mbar background pressure; 1.2 J/cm² under (d) 0.08 mbar, (e) 0.2 mbar, and (f) 0.54 mbar background pressure; 2 J/cm² under (g) 0.08 mbar, (h) 0.2 mbar, and (i) 0.54 mbar background pressure.

The dependency between PLD parameters and phase distribution according to Raman data follows the same conclusions made from GID data. But according to Raman data, the ε-phase is significantly weaker in samples deposited under pressure of 0.08 mbar and gets stronger in higher pressures, which is in contradiction to the Rietveld analysis made from θ-2θ measurements. One possibility for this is the fact that the measurement volume in Raman spectroscopy is very small unlike in XRD measurements, and the studied samples were not very homogenous. However, the Raman data is very consistent which improves its reliability, but straight comparison is impossible as Raman data only reveals the presence of a phase, not its percentage. On the other hand, the drawback of used θ-2θ XRD method is that it only recognizes specifically oriented nanoparticles. Because both GID and Raman data show similar tendency, it seems more likely, that the results of θ-2θ measurements are caused by orientation of the film, in addition to phase structure.

6.4.   Field Emission Scanning Electron Microscopy

Certain samples were chosen for FESEM studies to further determine the effect of PLD parameters on microstructure of deposited WO_3. Fig. 33 show that the size of the nanoparticles are in scale of 10-30 nm despite of the agglomerates being very large. Fig. 34 show that the WO_3 layer is up to 6 times thicker in samples deposited under

higher pressure, which is caused by the more porous structure. The effects of fluence and pressure were the same that were concluded from AFM micrographs, and effect of fluence was minor compared to pressure.
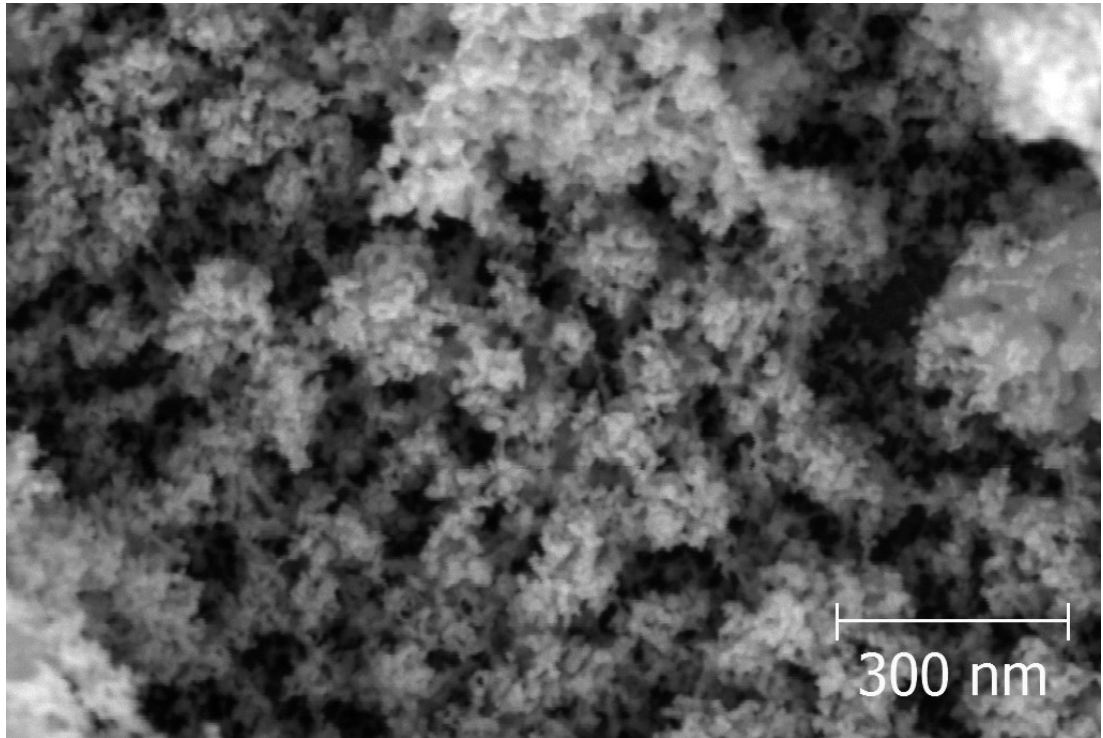

Figure 33. Top view FESEM micrograph of as-deposited sample using 0.88 J/cm² fluence under 0.54 mbar pressure.
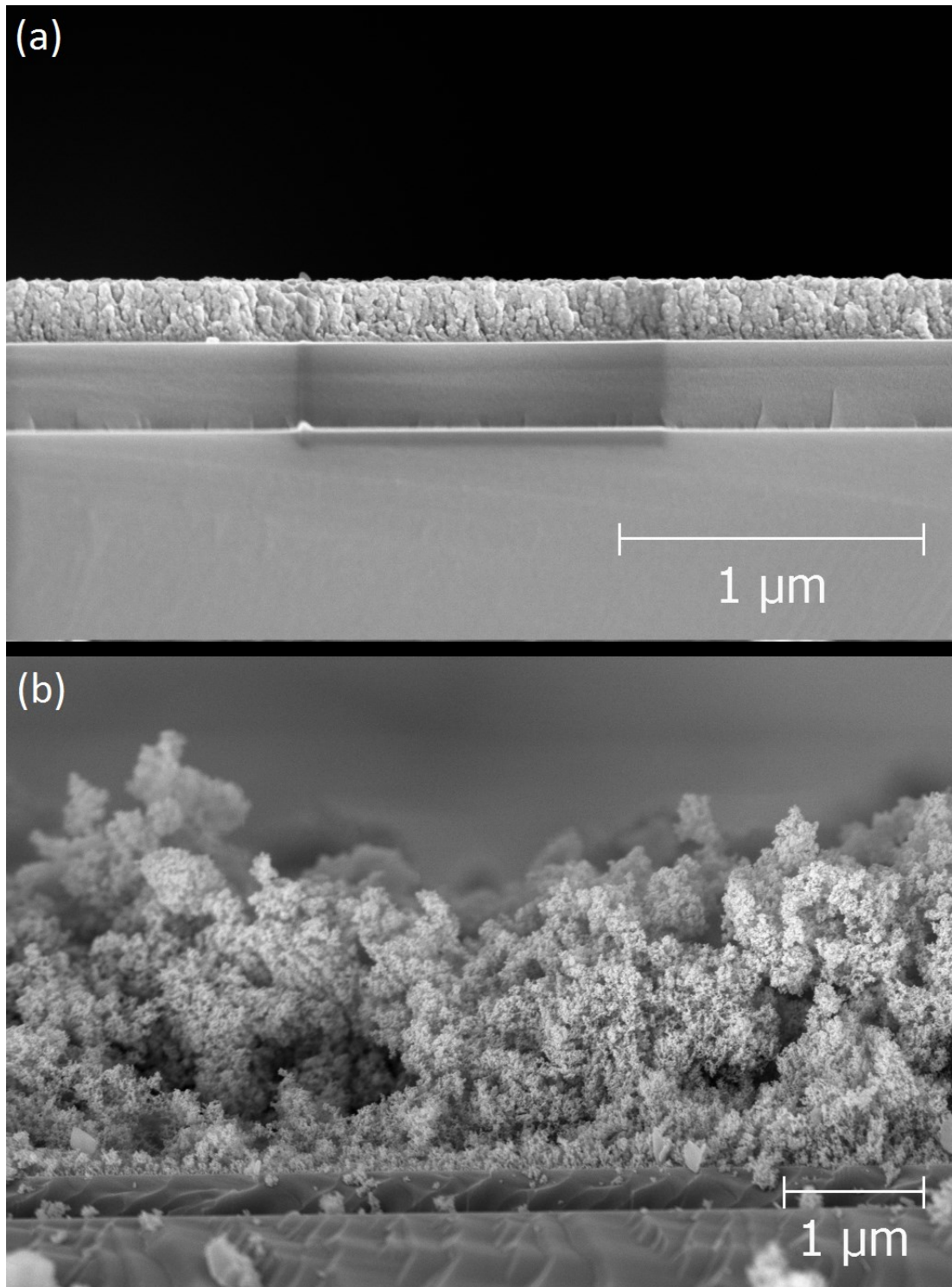
Figure 34. Cross-sectional FESEM micrographs of as-deposited samples using 1.2 J/cm² fluence under (a) 0.08 mbar and (b) 0.54 mbar pressure.

Post-annealing was found to have different effects depending on deposition parameters. From Fig. 35 it can be seen that, in low deposition pressure the nanoparticles have merged together and original microstructure has almost vanished, but in higher deposition pressure, the nanoparticles have only grown a bit, agglomerates have become denser, and the original microstructure is still present. The same phenomenon could be observed in other samples as well. Reason for this is most

likely caused by the difference in density before post-annealing as the WO_3 layer is much more porous in samples deposited under higher background pressure.
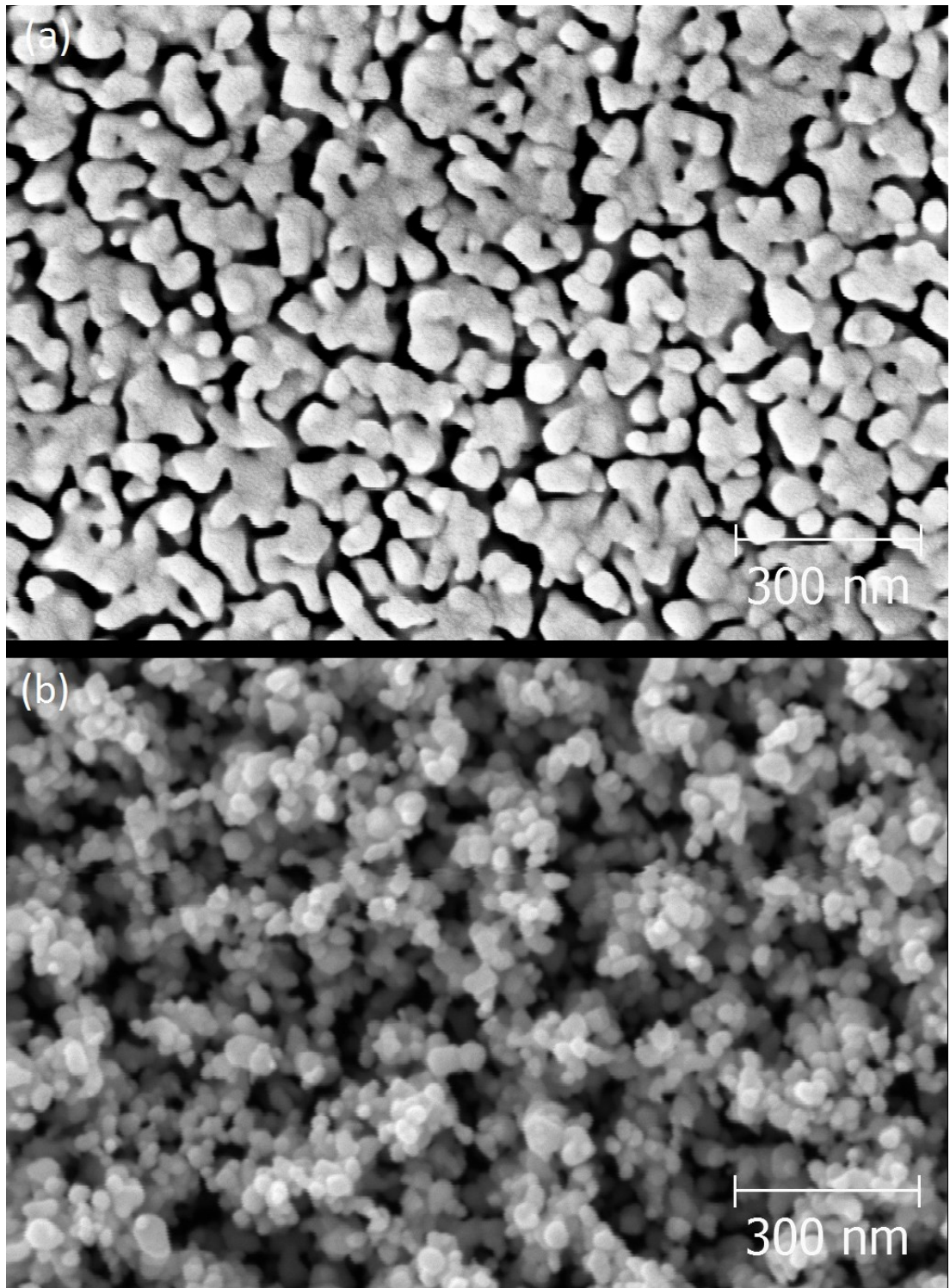

Figure 35. Top view FESEM micrographs of samples post-annealed at 500 °C using 1.2 J/cm² fluence under (a) 0.08 mbar and (b) 0.2 mbar pressure.

The effect of post-annealing temperatures can be observed in Fig. 36. From room temperature to 400 °C, the size of the nanoparticles remains the same and only the agglomerates shrink and tighten up. Shrinkage of agglomerates can be easily observed

in the gaps, which have grown wider and deeper uncovering parts of the surface of the substrate. The size of the nanoparticles has increased, as well. At 600 °C the effects are more of the same, but in addition some of the nanoparticles have started to form crystallites. Largest crystallites were up to few microns in length. The thickness of the WO_3 layer decreases as a function of post-annealing temperature as the agglomerates shrink and become denser.
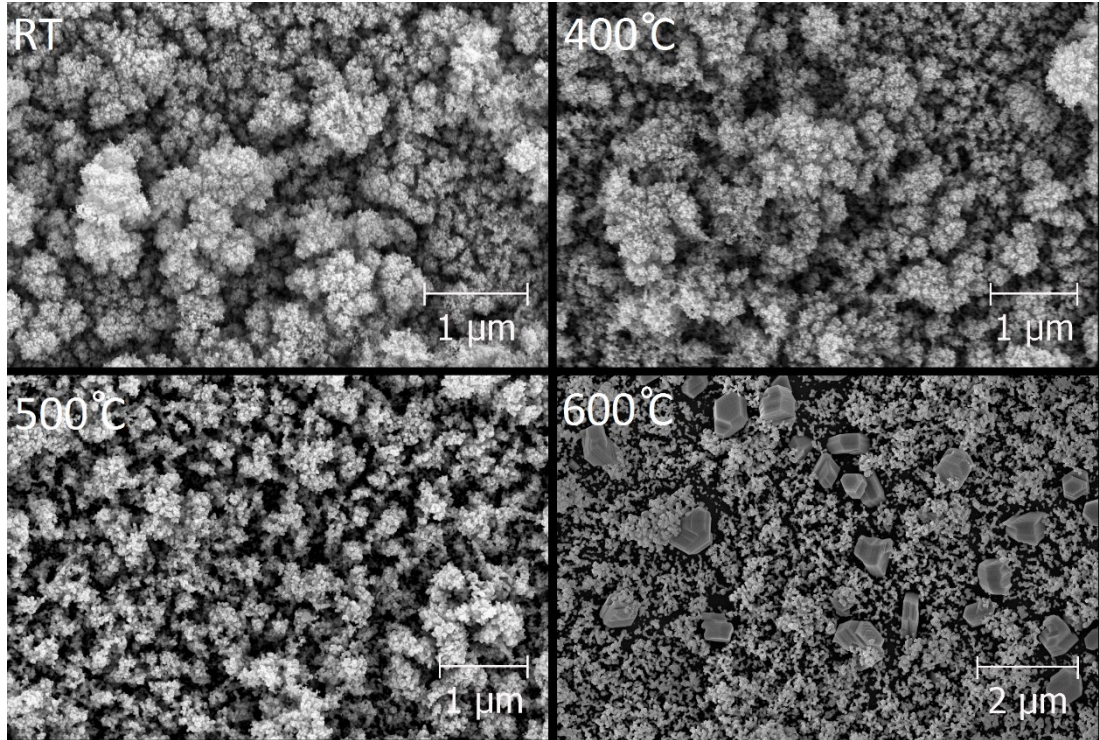
Figure 36. Top view FESEM micrographs of samples deposited using 0.88 J/cm² fluence under 0.2 mbar pressure with different post-annealing temperatures.

6.5. Gas Sensing Measurements

Gas sensing measurements were not in the focus of this thesis, but as an example one measurement is shown in Fig. 37. The data demonstrates good sensitivity to NO_x of the WO_3 films as even a ppm level concentration is enough to produce a response. It can also be seen how much different deposition pressure during PLD and different operation temperature can change the response signal.

Figure 37. NO$_x$ response of two different WO$_3$ films.

7. CONCLUSIONS

The objective of this thesis was to study the effects of laser beam fluence, pressure, and post-annealing temperature on microstructure of pulsed laser deposited tungsten trioxide th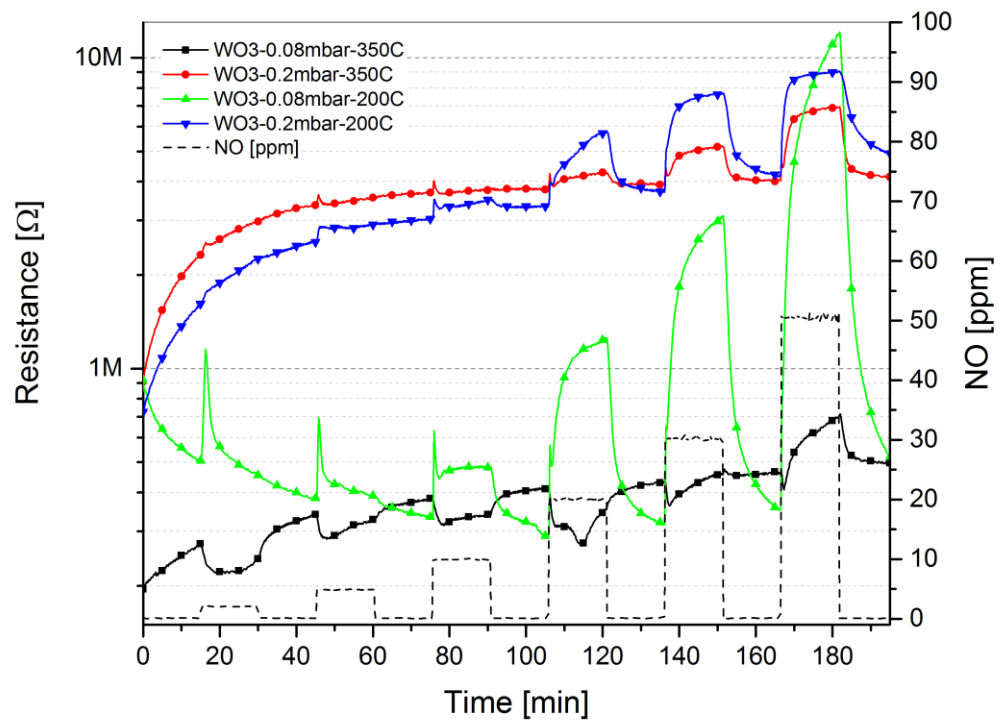in films. For these experiments, three different values of fluence and oxygen pressure, and four post-annealing temperatures were chosen, and set of samples was deposited to have one for every combination of processing parameters. Samples were measured using XRD, AFM, Raman spectroscopy, and FESEM to analyze the morphology and crystal structure of the films.

Surface and cross-section morphologies were found to consist of larger agglomerates, be more porous and rough when deposition pressure was increased. Fluence had an opposite, but much weaker impact. Post-annealing was found to shrink and compress agglomerates and eventually merge smaller structures together and even start a formation of large crystallites, but the effects were heavily dependent on the original morphology determined by fluence and background pressure. This makes it important to pay attention to each of the parameters when a certain type of morphology is wished to achieve. In this work, substrate to target distance was kept constant, but probably by altering it, the energy of the plasma can be changed and thus gain even better control over the morphology.

From the crystallographic studies, it was found that even though some crystallization takes place during the PLD, post-annealing is required to achieve proper crystallization degree. However, the crystallization process during post-annealing was not static, but dependent on the porosity of the film. The most porous film required higher temperature, but most likely a longer annealing time would have had similar effect.

The phase distribution and grain size were not unambiguous as the analysis of Raman and XRD data produced results that seemed different. Post-annealing temperature was found to increase the grain size and fluence had no significant impact on it, but the dependency of pressure was in contradiction. More measurements would be needed to clarify the exact numbers, but it is certain that the background pressure and post-annealing temperature indeed have an effect on both phase distribution and grain size. Neither set of data showed significant effect of fluence on phase structure or distribution.

The measurements proved that by altering the processing parameters, it is possible to control the thickness, density, and surface roughness of the deposited films, as well as grain size, crystallization degree, and phase structure of the deposited material. However, many of the effects are complex, non-linear and tied together so compromises must be made. To make a good gas sensor structural stability, small grain size and large effective surface area are desirable. Because gas sensors have high operation temperatures, even higher post-annealing temperature must be chosen, otherwise morphology and crystal structure of the film will go through changes when heated to operational temperature, and the results become unstable.

Identical WO_3 films have been used in gas sensing studies. It has been discovered that too low post-annealing temperature indeed leads to instability and that film deposited using 1.2 J/cm² under 0.2 mbar oxygen pressure and post-annealed in 400 °C was more selective to naphthalene than one deposited under 0.08 mbar [42]. In other experiment, the film under 0.08 mbar oxygen pressure was found to be more sensitive to nitrogen-oxides, carbon-monoxide, hydrogen, and ammonia than one deposited under 0.2 mbar. These studies prove that gas sensing abilities can be altered

by PLD processing parameters and that different applications require different properties of the film, which alone makes it important to know and understand the dependencies between PLD processing parameters and microstructure of the deposited film.

8. REFERENCES

[1] Yamazoe N. (2005) Toward innovations of gas sensor technology, Sensors and Actuators B: Chemical, Vol. 108, pp. 2-14.

[2] Tamaki J., Zhang Z., Fujimori K., Akiyama M., Harada T., Miura N., Yamazoe N. (1994) Grain-Size Effects in Tungsten Oxide-Based Sensor for Nitrogen Oxides, Journal of The Electrochemical Society, Vol. 141, pp. 2207-2210.

[3] Korotcenkov G. (2011) Chemical Sensors: Comprehensive Sensors Technologies. Volume 4: Solid-State Devices, Momentum Press, pp. 7-9.

[4] Chrisey D. B, Hubler G. K. (1994) Pulsed Laser Deposition of Thin Films, John Wiley & Sons Inc., pp. 3-11, 214, 231-235.

[5] Takehito Y., Takeyama S., Yamada Y., Mutoh K. (1996) Nanometer-sized silicon crystallites prepared by excimer laser ablation in constant pressure inert gas, Appl. Phys. Lett., Vol. 68, pp. 1772-1774.

[6] Schilling M., Guillaume A., Scholtyssek J. M., Ludwig F. (2014) Design of experiments for highly reproducible pulsed laser deposition of $YBa_2Cu_3O_{7-\delta}$, Journal of Physics D: Applied Physics, Vol. 47, pp. 293.

[7] Bäuerle D. (2000) Laser Processing and Chemistry, Springer, pp. 210, .460-462, 468-471, 638.

[8] Willmott P. R., Huber J. R. (2000) Pulsed laser vaporization and deposition, Reviews of Modern Physics, Vol. 72, pp. 315-328.

[9] Kelly R. (1989) On the dual role of the Knudsen layer and unsteady, adiabatic expansion in pulse sputtering phenomena, J. Chem. Phys., 92, pp. 5047-5056.

[10] Harilal S. S., Bindhu C. V., Tillack M. S., Najmabadi F., Gaeris A. C. (2003) Internal structure and expansion dynamics of laser ablation plumes into ambient gases, Journal of Applied Physics, 93, pp. 2380-2388.

[11] Infortuna A., Harvey A. S., Gauckler L. J. (2008) Microstructures of CGO and YSZ Thin Films by Pulsed Laser Deposition, Adv. Funct. Mater, 18, pp. 127-135.

[12] Koshizaki N., Narazaki A., Sasaki T. (2001) Size distribution and growth mechanism of Co_3O_4 nanoparticles fabricated by pulsed laser deposition, Scripta Materialia, Vol 44, pp. 1925-1928.

[13] Cantalini C., Pelino M., Sun H. T., Faccio M., Santucci S., Lozzi L., Passacantando M. (1996) Cross sensitivity and stability of NO_2 sensors from WO_3 thin film, Sensors and Actuators B 35-36, pp. 112-118.

[14] Dinda G. P., Shin J., Mazumder J. (2009) Pulsed laser deposition of hydroxyapatite thin films on Ti-6Al-4V: Effect of heat treatment on structure and properties, Acta Biomaterialia, Vol. 5, pp. 1821-1830.

[15] Fang Z. B., Yan Z. J., Tan Y. S., Liu X. Q., Wang Y. Y. (2005) Influence of post-annealing treatment on the structure properties of ZnO films, Applied Surface Science, Vol. 241, pp. 303-308.

[16] Manno D., Serra A., Di Giulio M., Micocci G., Tepore A. (1998) Physical and structural characterization of tungsten oxide thin film for NO gas detection, Thin Solid Films 324, pp. 44-51.

[17] Niklasson G. A., Granqvist C. G. (2007) Electochromics for smart windows: thin films of tungsten oide and nickel oxide, and devices based on these, J. Mater. Chem., 17, pp. 127-156.

[18] Carpenter M. A., Mathur S, Kolmakov A. (2013) Metal Oxide Nanomaterials for Chemical Sensors, Springer New York 2013, pp. 176-183.

[19] Wang L., Teleki A., Pratsinis S. E., Gouma P. I. (2008) Ferroelectric WO_3 Nanoparticles for Acetone Selective Detection, Chem. Matter., 20, pp. 4794-4796.

[20] Johansson M. B., Baldissera G., Valyukh I., Persson C., Arwin H., Niklasson G. A., Österlund L. (2013), Electronic and optical properties of nanocrystalline WO_3 thin films studied by optical spectroscopy and density functional calculations, J. Phys.: Condens. Matter, Vol. 25

[21] Lappalainen J., Viter R., Puustinen J., Gornostayev D., Smyntyna V. (2010) PLD-grown WO_3 nanostructures with ε-phase for gas sensor applications, Procedia Engineering 5, pp. 343-346.

[22] Kim T. S., Yong B. K., Kwang S. Y., Sung G. S., Hyung J. J. (2000) Sensing characteristics of dc reactive sputtered WO_3 thin films as an NO_x gas sensor, Sensors and Actuators B 62, pp. 102-108.

[23] Meyer E., Hug H. J., Bennewitz R. (2004) Scanning Probe Microscopy: The Lab on a Tip, Springer, pp. 2-13, 87-90.

[24] Veeco Ltd (2005) A Practical Guide to Scanning Probe Microscopy.

[25] Peyronel M. F., Marangoni A. G. (2014) Analytical Methods, Procedures and Theory for the Physical Characterization of Fats Section 1: X-ray Powder Diffractiometery (XRD), The AOCS Lipid Library.

[26] Waseda Y., Matsubara E., Shinoda K. (2011) X-Ray Diffraction Crystallography: Introduction, Examples and Solved Problems, Springer, pp. 73-75, 125.

[27] Mitsunaga T. (2009) X-ray thin-film measurement techniques chap. II. Out-of-plane diffraction measurements, The Rigaku Journal, 25, pp. 7-12.

[28] Colthup N. (1975) Introduction to Infrared and Raman Spectroscopy: 2nd edition, Academic Press Inc., pp. 57-59.

[29] Bennett J. M., Mattsson L. (1999) Introduction to Surface Roughness and Scattering – Second Edition, Optical Society of America, pp. 58-62.

[30] Woodward P. M., Sleight A. W., Vogt T. (1995) Structure Refinement of Triclinic Tungsten Trioxide, J. Phys. Chem. Solids., Vol 56, pp. 1305-1315.

[31] Salje E. K. H., Rehmann S., Pobell F. (1997) Crystal structure and paramagnetic behaviour of $\varepsilon\text{-}WO_{3-x}$, J. Phys.: Condens. Matter, Vol 9, pp. 6563-6577.

[32] Saha D., Jensen K. M. Ø., Tyrsted C., Bøjesen D. E., Mamakhel A. H., Dippel A-C., Christensen M., Iversen B. B. (2014) In Situ Total X-Ray Scattering Study of WO_3 Nanoparticle Formation under Hydrothermal Conditions, Angew. Chem. Int., 53, pp. 3667-3670.

[33] Rietveld H. M. (1968) A Profile Refinement Method for Nuclear and Magnetic Structures, J. Appl. Cryst., 2, pp. 65-71.

[34] Warren B. E., Averbach B. L. (1950) The Effect of Cold-Work Distortion on X-Ray Patterns, J. Appl. Phys., Vol 21, pp. 595-599.

[35] Williamson G. K., Hall W. H. (1953) X-ray line broadening from filed aluminium and wolfram, Acta Metallurgica, Vol 1, pp. 22-31.

[36] Krumm S. (1994) WINFIT 1.0 – A Computer Program for X-ray Diffraction Line Profile Analysis, Acta Universitatis Carolinae Geologica 38, pp. 253-261.

[37] Souza Filho A. G., Freire P. T. C., Pilla O., Ayala A. P., Mendes Filho J., Melo F. E. A., Freire V. N., Lemos V. (2000) Pressure effects in the Raman spectrum of WO_3 microcrystals, Physical Review B, Vol. 62, pp. 3699-3703.

[38] Cazzanelli E., Vinegoni C., Mariotto G., Kuzminà A., Purans J. (1999) Low-Temperature Polymorphism in Tungsten Trioxide Powders and Its Dependence on Mechanical Treatments, Journal of Solid State Chemistry 143, pp. 24-32.

[39] Lee S-H., Cheong H. M., Liu P., Smith D., Tracy C. E., Mascanrenhas A., Pitts J. R., Deb S. K. (2000) Gasochromic mechanism in α-WO_3 thin films based on Raman spectroscopic studies, Journal of Applied Physics, Vol. 88, pp. 3076-3078.

[40] Santo N., Filipescu M., Ossi P. M., Dinescu M. (2010) Nanostructure evolution in cluster-assembled WO_x films synthesized by radio-frequency assisted laser ablation, Applied Physics A: Materials Science & Processing, 101, pp. 325-331.

[41] Kumar V. B., Mohanta D. (2010) Formation of nanoscale tungsten oxide structures and colouration characteristics, Bull. Mater. Sci., Vol. 34, pp. 435-442.

[42] Leidinger M., Huotari J., Sauerwald T., Lappalainen J., Schütze A. (2015) Nanostructuder WO_3 Semiconductor Gas Sensors for Selective Detection of Naphthalene, AMA conferences 2015 – SENSORS 2015 and IRS2 2015, 19-21 May 2015, Nürnberg, Germany, Proceedings SENSOR 2015 (DOI 10.5162/sensors2015/E8.2) (ISBN 978-3-9813484-8-4).